

A DEEP LY α SURVEY IN ECDF-S AND COSMOS: I. GENERAL PROPERTIES OF LY α EMITTERS AT $Z \sim 2$

CAI-NA HAO,¹ JIA-SHENG HUANG,^{2,3} XIAOYANG XIA,¹ XIANZHONG ZHENG,⁴ CHUNYAN JIANG,⁵ AND CHENG LI⁶

¹*Tianjin Astrophysics Center, Tianjin Normal University, Tianjin 300387, China*

²*National Astronomical Observatories, Chinese Academy of Sciences, Beijing 100012, China*

³*Harvard-Smithsonian Center for Astrophysics, 60 Garden Street, MS65, Cambridge, MA 02138, USA*

⁴*Purple Mountain Observatory, Chinese Academy of Sciences, Nanjing 210008, China*

⁵*Key Laboratory for Research in Galaxies and Cosmology of Chinese Academy of Sciences, Shanghai Astronomical Observatory, Shanghai 200030, China*

⁶*Physics Department and Tsinghua Center for Astrophysics, Tsinghua University, Beijing 100084, China*

Submitted to ApJ

ABSTRACT

Ly α Emitters (LAEs) may represent an important galaxy population in the low mass regime. We present our deep narrowband imaging surveys in the COSMOS and ECDF-S fields and study the properties of LAEs at $z = 2.23 \pm 0.03$. The narrowband surveys conducted at Magellan II telescope allow us to obtain a sample of 452 LAEs reaching a 5σ limiting magnitude of ~ 26 mag. Our Ly α luminosity functions extend to $10^{41.8}$ erg s $^{-1}$ with steep faint-end slope. Using multi-wavelength ancillary data, especially the deep *Spitzer*/IRAC 3.6 μ m and 4.5 μ m photometric data, we obtained reliable stellar mass estimates for 130 IRAC-detected LAEs, spanning a range of $8 < \log(M_*/M_\odot) < 11.5$. For the remaining IRAC-undetected LAEs, the median-stacked spectral energy distribution yields a stellar mass of $\log(M_*/M_\odot) = 7.97^{+0.05}_{-0.07}$ and the rest-frame ultraviolet emission indicates a median star formation rate of $\log(SFR/M_\odot \text{ yr}^{-1}) = -0.14 \pm 0.35$. There are six LAEs detected by the *Spitzer*/MIPS 24 μ m or even *Herschel* far-infrared observations. Taking into account the six MIR/FIR detected LAEs, our LAEs cover a wide range in the star formation rate ($1 < \text{SFR} < 2000 M_\odot \text{ yr}^{-1}$). Although LAEs as a population are diverse in their stellar properties, they are mostly low-mass star-forming galaxies and follow the star formation main sequence relations or their extrapolations to the low-mass end, implying a normal star-forming nature of LAEs. The clustering analysis indicates that our LAEs reside in dark matter halos with $\langle \log(M_h/M_\odot) \rangle = 10.8^{+0.56}_{-1.1}$, suggesting that they are progenitors of local Large Magellanic Cloud-like galaxies.

Keywords: galaxies: evolution - galaxies: formation - galaxies: high-redshift - galaxies: luminosity function - galaxies: star formation

1. INTRODUCTION

The epoch at $z \sim 2$ is crucial in the history of galaxy evolution when the cosmic star formation rate density (SFRD) reaches its peak (Madau & Dickinson 2014, and references therein). Detailed knowledge of massive ($> 10^{10} M_{\odot}$) galaxies at this epoch has been widely investigated (e.g., Erb et al. 2006; Förster Schreiber et al. 2009; Steidel et al. 2014; Kriek et al. 2015; Burkert et al. 2016; Wuyts et al. 2016). On the other hand, low-mass galaxies at $z \sim 2$ pose a unique and important position in studying galaxy evolution because they are building blocks of local mature galaxies. However, our knowledge on low-mass galaxies ($< 10^{10} M_{\odot}$) at $z \sim 2$ is still limited due to challenges in identifying these faint galaxies. Large samples, on the other hand, are needed for a robust census of such galaxies. The narrowband imaging technique is an effective way of detecting Ly α emitting galaxies (LAEs) at specific redshifts (e.g., Malhotra & Rhoads 2002; Wang et al. 2005; Finkelstein et al. 2007, 2008; Gawiser et al. 2007; Gronwall et al. 2007; Nilsson et al. 2007; Pirzkal et al. 2007; Lai et al. 2008; Ono et al. 2010a,b; Acquaviva et al. 2011; Zheng et al. 2016). Other methods such as integral-field spectroscopy (e.g., van Breukelen et al. 2005; Drake et al. 2017), slit spectroscopy (e.g., Rauch et al. 2008) and medium-band imaging (e.g., Stiavelli et al. 2001; Taniguchi et al. 2015; Sobral et al. 2018) have also been employed in finding LAEs. LAEs were found to be mostly composed of low-mass star-forming galaxies (e.g., Gawiser et al. 2006; Finkelstein et al. 2007; Lai et al. 2008; Pirzkal et al. 2007; Nilsson et al. 2011; Guaita et al. 2011; Shimakawa et al. 2017), red massive star-forming LAEs exist though (e.g., Stiavelli et al. 2001; Lai et al. 2008; Finkelstein et al. 2008, 2009; Ono et al. 2010b; Acquaviva et al. 2011; Guaita et al. 2011; Nilsson et al. 2011; Oteo et al. 2012;

Matthee et al. 2016). Therefore, LAEs can be used to probe the properties of low-mass galaxies at high redshifts.

In the past several years, a number of narrow-band imaging surveys and spectroscopic observations have been carried out to search for LAEs at $z \sim 2$ (e.g., Nilsson et al. 2009; Guaita et al. 2010; Nakajima et al. 2012; Blanc et al. 2011; Cassata et al. 2011; Hathi et al. 2016; Matthee et al. 2016; Shimakawa et al. 2017). These surveys and deep multi-wavelength ancillary data have made it possible to yield measurements of properties of LAEs such as Ly α luminosity function, star formation rate, stellar mass, dark matter halo mass and rest-frame optical spectroscopic properties etc (e.g., Guaita et al. 2011; Nilsson et al. 2011; Ciardullo et al. 2012, 2014; Guaita et al. 2013; Nakajima et al. 2013; Trainor et al. 2016; Sobral et al. 2017; Kusakabe et al. 2018).

The Ly α luminosity function and its faint-end slope are of special interest since they can serve as probes of galaxy evolution and cosmic reionization (e.g., Rauch et al. 2008; Konno et al. 2016; Zheng et al. 2017). In order to determine the faint-end slope of the Ly α luminosity function, many surveys have been carried out to detect LAEs with much faint luminosities (e.g., Blanc et al. 2011; Ciardullo et al. 2012). Based on a deep spectroscopic survey, Cassata et al. (2011) put strong constraints on the faint-end slope of the Ly α luminosity functions at $1.95 < z < 3$ and $3 < z < 4.55$. They ruled out a flat slope of ~ -1 at 5σ and 6.5σ levels at these two redshift ranges, and specifically obtained a slope of -1.6 ± 0.12 for the Ly α luminosity function at $z \sim 2.5$. More recently, a wide-field (1.43 deg^2) Subaru Ly α survey with an unprecedented depth obtained a much larger LAE sample of >3000 galaxies at $z = 2.2$ (Konno et al. 2016). This sample yields an even steeper slope of $-1.75^{+0.10}_{-0.09}$ at $z \sim 2$. Later on, the steep slope was confirmed by another wide-field sur-

vey (1.43 deg^2) at similar redshifts but with shallower narrowband exposures (Sobral et al. 2017). All those surveys indicated that there are more galaxies at faint luminosity end, and their volume densities are much higher than those with higher luminosities.

Among others, stellar mass is one of the most difficult quantities to be measured due to their faint continuum. Usually it requires the rest-frame long wavelength optical or near-infrared (NIR) photometry to determine a reliable galaxy stellar mass. For an LAE at $z > 2$, its rest-frame long wavelength optical and NIR continua move to NIR or mid-IR (MIR) bands. Nonetheless, an LAE appears to be very faint in NIR and MIR. A typical LAE at $z \sim 2$ would have a R -band magnitude of 25.3–25.5 magnitude (Guaita et al. 2010; Vargas et al. 2014) and a flat Spectral Energy Distribution (SED). Thus its NIR or MIR magnitude will also be 25.5 magnitude or even fainter. There are only $\sim 20\% - 30\%$ of luminous LAEs detected at $3.6 \mu\text{m}$, $4.5 \mu\text{m}$ in the deep Spitzer IRAC surveys (Nilsson et al. 2011). It requires a large and deep coverage in NIR or MIR to detect faint LAEs and measure their stellar masses.

Furthermore, star formation rate (SFR) and stellar mass were found to have a tight correlation for normal star-forming galaxies, called the star formation “main sequence” (SFMS) (e.g., Brinchmann et al. 2004; Elbaz et al. 2007), which defines a steady star formation mode. Starburst galaxies are located above the SFMS relation (e.g., Rodighiero et al. 2011). At high redshifts, the SFMS relation is derived mainly based on galaxies with stellar mass larger than $10^{10} M_{\odot}$ (e.g., Daddi et al. 2007; Rodighiero et al. 2011; Fang et al. 2012; Shivaee et al. 2015, 2017), and it is often extrapolated to low mass to be compared with LAEs. There is a debate on the locations of LAEs relative to the SFMS relation, i.e. the existing studies found that LAEs lie above (Guaita et al.

2013; Hagen et al. 2014, 2016; Vargas et al. 2014; Oteo et al. 2015) or on (Shimakawa et al. 2017; Kusakabe et al. 2018) the SFMS. It was suggested that the inconsistent results may be caused by different survey depths or the use of different extinction curves (Shimakawa et al. 2017; Kusakabe et al. 2018).

Different survey depths of both narrowband and broadband observations would result in different sample selection effects and sample properties. Therefore, large and deep coverage in both narrowband and broadband is needed to provide further independent constraints. In this paper series, we will study the properties of LAEs using a deep narrowband-selected LAE sample with deep multi-wavelength data. We specifically designed a customized narrowband filter at 3928 \AA with filter width of 70 \AA (see Figure 1) for detections of LAEs at $z = 2.23 \pm 0.03$. At the same redshift, $H\alpha$ emitters can be selected using the typical NIR narrowband filter at $2.12 \mu\text{m}$ widely available on many telescopes (Geach et al. 2008; Sobral et al. 2013; An et al. 2014). So this filter design permits a comparison between $\text{Ly}\alpha$ and $H\alpha$ selection for galaxy populations at $z = 2.23$ (e.g., Matthee et al. 2016; An et al. 2017; Sobral et al. 2017). We chose the COSMOS and ECDF-S fields, where deep *HST* imaging data are available including the Galaxy Evolution from Morphologies and SEDs (GEMS; Rix et al. 2004), the Cosmic Evolution Survey (COSMOS; Scoville et al. 2007), and the Cosmic Assembly Near-IR Deep Extragalactic Legacy Survey (CANDELS; Grogin et al. 2011; Koekemoer et al. 2011). Both fields were also covered in MIR by the *Spitzer* Extended Deep Survey (SEDS; Ashby et al. 2013). The deep *Spitzer* and *HST* imaging data allow us to study the stellar masses and SFMS in this paper and UV morphologies in a forth-coming paper (Hao et al. 2018, in preparation). Our narrowband observations were carried out on Magellan II

telescope with excellent seeing condition, making it possible to study morphologies of Ly α emission (Huang et al. 2018, in preparation).

This paper is structured as follows. In Section 2, we describe observations and data reduction. Selection of LAEs is presented in Section 3. We have our main results in Section 4 and 5, and conclude in Section 6. We adopt a flat Λ CDM cosmology with $\Omega_m = 0.3$, $\Omega_\Lambda = 0.7$, $H_0 = 70 \text{ km s}^{-1} \text{ Mpc}^{-1}$ and $\sigma_8 = 0.8$ for all calculations, and a Salpeter Initial Mass Function (IMF; Salpeter 1955) for stellar population analysis.

2. OBSERVATIONS AND DATA REDUCTION

2.1. Observations

The NB3928 \AA imaging observations of the COSMOS and ECDF-S fields were conducted with Megacam on the 6.5m Magellan II telescope. Megacam is a wide-field mosaic CCD camera with 9×4 CCD arrays, each of which has 2048×4608 pixels. The focus ratio (F/5) for Megacam on Magellan leads to a pixel scale of $0''.08/\text{pixel}$, and thus an effective field-of-view of $\sim 24' \times 24'$. We used a binning of 2×2 for a faster readout, yielding an actual pixel scale of $0''.16/\text{pixel}$. The observations were executed using dithering mode with single exposure of 15 minutes to minimize the number of saturated stars¹ in each exposure. The dithering steps vary from $-49''$ to $63''$ to fill in the chip gaps. During the narrowband observations, the seeing spans a range of $0.5''$ - $1.0''$ ², but mostly smaller than $0.7''$. The resultant median seeing is $0.6''$. After rejecting a few raw images with unusually high sky background, we obtained total exposures of 600 and 660 minutes respectively in the

¹ Stars are saturated at a narrowband magnitude of 15.4 mag.

² There is only one image with a seeing larger than $1.0''$, and it was rejected.

COSMOS and ECDF-S fields. The observation parameters are summarized in Table 1.

2.2. Data Reduction

The data reduction was performed with a combination of IRAF mscred package and the customized package Megared developed in CfA/Harvard³. The science images were first bias- and dark-corrected, then flat-fielded. The flat field was generated using the twilight flat taken in this run. We then removed the residual pattern in each reduced frame by subtracting each frame with the mean background frame, which was produced by stacking all science frames after removing all objects on them.

The WCS solution for each science image needs to be refined based on the preliminary WCS solution assigned in the observations. We used the CfA/Harvard developed TCL script “megawcs” to correct distortion and relative array placement of each frame. The reference positions used in this correction were those of bright objects taken from the *HST*/ACS *I*-band catalog in COSMOS (Capak et al. 2007; Ilbert et al. 2009) and the GEMS *HST*/ACS *V*-band catalog in ECDF-S (Caldwell et al. 2008). Position offsets for these objects in the refined images and the reference catalogs are plotted in Figure 2 with standard deviations of $0''.16$ and $0''.17$ respectively in COSMOS and ECDF-S. The accurate WCS in each image permits optimization of the PSF in the final stacked image.

Photometric zero point in each observed frame varies due to the changes of photometric conditions during the observations. Because we cover only one field of view with dithers in each field, we are able to use one set of bright stars in each field to normalize zero point in each exposure to a reference frame. A reference frame is one taken under the photometric condition with airmass ~ 1 . We measured flux densi-

³ <https://www.cfa.harvard.edu/mashby/megacam/megacam>

ties of those bright objects in each single frame and compared them with those in the reference image. A median flux ratio was calculated for each frame, and this ratio was used to normalize photometric zero point of each frame to that of the reference frame before stacking. Finally, these images were mosaiced into a single frame using Swarp software (Bertin et al. 2002). A coverage map was also generated accordingly in each field. The Full Width at Half Maximum (FWHM) for PSFs of the final stacked science images in both fields is $0''.57$. The effective coverages for the two fields are nearly the same, each $\sim 26'.9 \times 26'.9$.

The absolute flux calibration was done using archival U and B band images in COSMOS and ECDF-S. Specifically, CFHT u^* and Subaru B_J from the COSMOS archive⁴ (Capak et al. 2007) and ESO MPG Wide Field Imager (WFI) U and B band images from the Multi-wavelength Survey by Yale-Chile (MUSYC) archive⁵ (Taylor et al. 2009; Cardamone et al. 2010) were used for the COSMOS and the ECDF-S fields respectively. The central wavelength of our N3928 Å narrowband filter is in between the U and B bands, so a linear interpolation of U and B band fluxes at the central wavelength of N3928 Å can be used as the underlying continuum of the Ly α emission (Nilsson et al. 2009; Guaita et al. 2010). Following Guaita et al. (2010), we derived the fractional contributions from U and B band flux densities, taking account of the central wavelengths of the filters (see section 2.3). Finally, by assuming that the median color excess (see section 3) of all objects is zero, the zero point of the N3928 Å image was derived. However, as noted by Sobral et al. (2017), a narrowband filter like ours covers the strong stellar CaHK absorption feature. A blind use of objects with-

out considering their spectral types could introduce problems. So we searched for counterparts of our narrowband-detected objects in the 3D-HST catalogs (Skelton et al. 2014) and selected star-forming galaxies using the UVJ method (Williams et al. 2009; Brammer et al. 2011) based on the rest-frame $U - V$ and $V - J$ colors provided by the 3D-HST catalogs. It turned out that the narrowband zero point based on star-forming galaxies is consistent with that obtained using all objects. This implies that our narrowband-detected objects are not dominated by objects with strong stellar CaHK absorption. The 5σ limiting magnitudes in a $3''$ diameter aperture in the narrowband images are 25.97 and 26.02 mag for the COSMOS and ECDF-S fields, respectively.

2.3. Photometry

We detected objects from the narrowband image using SExtractor software (Bertin & Arnouts 1996). Objects with a minimum of 11 adjacent pixels above a threshold of 1.5σ per pixel were selected. The coverage map was used as the weight image to depress spurious detections. Aperture magnitudes with circular apertures of diameters of 8 pixels, ~ 2 FWHM of seeing disks, were measured. We then made aperture corrections to obtain the total fluxes using the growth curve derived from bright stars. We note that such aperture corrections are made by assuming that the objects are point-like sources. Such an assumption is reasonable for the vast majority of our LAEs (Huang et al. 2018, in preparation). We note that MAG_AUTO from SExtractor is often used to measure the total Ly α fluxes in the literature. However, the fluxes measured by MAG_AUTO are dependent on the survey depth and are biased measurements for faint objects near the detection limits, as noted by Matthee et al. (2016) and Konno et al. (2014). This was also seen in our data. We found that the aperture-corrected fluxes under-estimate the total fluxes

⁴ <http://irsa.ipac.caltech.edu/data/COSMOS>

⁵ <http://www.astro.yale.edu/MUSYC>

probed by MAG_AUTO only for bright LAEs, while the MAG_AUTO fluxes for LAEs with $NB > 25\text{mag}$ are consistent with the aperture-corrected fluxes on average but with larger photometric errors. Therefore, we decided to use the aperture-corrected flux as a measure of the total flux in the following analysis. The exception is that MAG_AUTO was also used in the construction of Ly α luminosity functions (See section 4) for the purpose of comparisons with studies in the literature.

Objects with signal-to-noise ratio less than 5 in the narrowband photometry were excluded. But objects fainter than the 5σ limiting magnitude were not removed from the catalog. We masked out saturated stars and high noise area (with exposure time ≤ 40 minutes) in the narrowband images. The objects located in the masked area were accordingly removed from the final catalog. The final narrowband photometry catalogs consist of 25,756 and 27,946 objects, covering effective area of 602.05 and 612.75 arcmin² in the COSMOS and ECDF-S fields, respectively.

For the calculation of the narrow-to-broad band color excess, we re-binned the U and B band images to match the pixel scale of the narrowband image in each field and then performed aperture photometry on the broadband images using SExtractor software in “dual image” mode. The narrowband image was used as the detection image and the broadband images were taken as measurement images. We used the same set-up in the “dual image” mode as that used for the source detection, as listed above. The seeing FWHM of U and B band images are $0''.87$ and $0''.94$ for COSMOS and $1''.03$ and $1''.02$ for ECDF-S. Circular aperture photometry with diameters of 12 (14) pixels was carried out on both U and B band images for the COSMOS (ECDF-S) field. For some objects detected in the narrowband, the measured broadband fluxes have signal-to-noise ratio less

than 2. We then used 2σ flux limits for these objects. Similar to the narrowband case, aperture corrections were subsequently made to measure the total fluxes using the growth curves obtained from bright stars in U and B bands. Aperture corrected magnitudes were used to calculate the narrow-to-broad band color excess.

After the photometry in both narrowband and its adjacent broadbands was obtained, the underlying continuum of the Ly α line, denoted by $f_{\lambda,UB,con}$, the Ly α equivalent width (EW) and the Ly α line flux could be calculated. Since the broadband observations of the two fields used different filters, we adopted different equations to calculate these quantities. As mentioned in Section 2.2, we used a linear combination of U and B band flux densities to measure the continuum with the central wavelengths of the filters taken into account. Specifically, the interpolated U and B band flux densities at the narrowband central wavelength is derived via the linear interpolation formula

$$\frac{f_{\lambda,UB} - f_{\lambda,U}}{\lambda_{NB} - \lambda_U} = \frac{f_{\lambda,B} - f_{\lambda,U}}{\lambda_B - \lambda_U}, \quad (1)$$

where $f_{\lambda,UB}$ is the interpolated U and B band flux densities at the narrowband central wavelength, $f_{\lambda,U}$ and $f_{\lambda,B}$ are the U and B band flux densities, while λ_{NB} , λ_U and λ_B are the central wavelengths of the narrowband, U and B band filters, respectively. For COSMOS, $f_{\lambda,UB} = 0.80f_{\lambda,U} + 0.20f_{\lambda,B}$, while for ECDF-S, $f_{\lambda,UB} = 0.57f_{\lambda,U} + 0.43f_{\lambda,B}$. For the COSMOS field, we note that the CFHT U band filter includes the Ly α line (See the left panel of Figure 1). Therefore, we need to remove the Ly α emission from the observed U band flux density before it is used to calculate the underlying continuum. For LAEs in COSMOS, the equation used to calculate the continuum of the Ly α line is:

$$f_{\lambda,UB,con} = \frac{f_{\lambda,UB} - 0.80f_{\lambda,N393} \frac{\Delta\lambda_{NB}}{\Delta\lambda_U}}{1 - 0.80 \frac{\Delta\lambda_{NB}}{\Delta\lambda_U}}, \quad (2)$$

where $f_{\lambda,N393}$ is the narrowband flux density, while $\Delta\lambda_{NB}$ and $\Delta\lambda_U$ are the bandwidth of the narrowband and U band filters, respectively. Accordingly, the EW for LAEs in the COSMOS field can be derived using the following equation:

$$EW_{\text{obs}} = \frac{f_{\lambda,N393} - f_{\lambda,UB}}{f_{\lambda,UB} - f_{\lambda,N393} \frac{0.80\Delta\lambda_{NB}}{\Delta\lambda_U}} \Delta\lambda_{NB}, \quad (3)$$

where EW_{obs} is the observed EW that is related to the rest-frame EW by $EW_{\text{obs}} = (1+z)EW_{\text{rest}}$. The Ly α flux is obtained as follows:

$$F(\text{Ly}\alpha) = \frac{f_{\lambda,N393} - f_{\lambda,UB}}{1 - 0.80 \frac{\Delta\lambda_{NB}}{\Delta\lambda_U}} \Delta\lambda_{NB}. \quad (4)$$

For the case of the ECDF-S field, the calculations of $f_{\lambda,UB,con}$, Ly α EW and Ly α line flux are simpler since the Ly α line is not included in the broadband filters. So for LAEs in ECDF-S,

$$f_{\lambda,UB,con} = f_{\lambda,UB}, \quad (5)$$

$$EW_{\text{obs}} = \frac{f_{\lambda,N393} - f_{\lambda,UB}}{f_{\lambda,UB}} \Delta\lambda_{NB}, \quad (6)$$

and the Ly α flux is derived using the following equation:

$$F(\text{Ly}\alpha) = (f_{\lambda,N393} - f_{\lambda,UB}) \Delta\lambda_{NB}. \quad (7)$$

2.4. Survey Completeness

It is essential to determine the completeness of the narrowband surveys. The Monte Carlo simulations were employed to measure the narrowband survey completeness in both fields respectively. We first selected several tens of bright stars (SExtractor parameter CLASS_STAR ≥ 0.95) with the aperture-corrected narrowband magnitudes $19 \leq NB < 22$ mag in both fields, scaled down their flux densities, and put back in random locations in their original images. SExtractor with the same parameter set was run again on the images with artificial objects. This simulation was performed several hundred times

to achieve adequate statistics in each magnitude bin. Completeness of the narrowband detections in both fields was measured as the artificial object recovery rate in each magnitude bin, shown as the solid data points in Figure 3. The 90% and 50% completeness limits are 25.50 mag and 25.99 mag for the COSMOS field and 25.78 mag and 26.20 mag for the ECDF-S field.

3. SELECTION OF LAE CANDIDATES

Selection of LAEs is generally based on their emission line EW. Practically the narrowband-to-broadband color excess (i.e., magnitude difference) can be used as a proxy. We use UB as magnitude for the interpolated U and B bands flux density, and NB as narrowband magnitude. The median NB-UB should be zero for galaxies with no line shifting to the band. When a line shifts to the narrowband, the NB-UB appears “blue”. We plot NB-UB against NB in Figure 4. The scatters in NB-UB come from the NB, U , and B band photometry uncertainties. We measured the rms scatters σ_{NB-UB} in the NB-UB distributions as a function of NB magnitude and used $3\sigma_{NB-UB}$ as the threshold to select narrowband excess sources as LAE candidates. Due to the different depths in broadband photometry in these two fields, EWs calculated using $3\sigma_{NB-UB}$ are slightly different, $\sim 20 \text{ \AA}$ in COSMOS and $\sim 30 \text{ \AA}$ in ECDF-S respectively. If a selection criterion of $EW \geq 30 \text{ \AA}$ is used for COSMOS, the number densities and main results do not change significantly (see below for details). This selection left us with 212 LAEs in COSMOS and 263 LAEs in ECDF-S shown in Figure 4.

The narrowband-excess sample yielded by the single NB-UB selection also includes objects with emission lines other than Ly α line redshifting to our narrowband filter waveband. For example, [O II] at $z \sim 0.05$; Al III at $z \sim 1.1$; C III] at $z \sim 1.06$; C IV at $z \sim 1.5$; and Si IV + O IV at $z \sim 1.8$ etc. Among these lines, only [O II] appears in a normal galaxy spectrum,

while the remaining high ionization lines appear in active galactic nuclei (AGNs) spectra. The [O II] emitters are at such a low redshift that they occupy too small volume to actually contribute to the selected sample. Those high ionization line emitters were identified using X-ray catalogs (Civano et al. 2012; Luo et al. 2008; Lehmer et al. 2005; Virani et al. 2006) and spectroscopic information from NED⁶. We identified 16 broad-line AGNs and one candidate AGN with X-ray emission at $z = 1.694$ (Salvato et al. 2011) in COSMOS, and 7 broad-line AGNs in ECDF-S in the narrowband-excess sample. Four of the broad-line AGNs in COSMOS (Trump et al. 2009; Civano et al. 2012) and 2 in ECDF-S (Treister et al. 2009; Silverman et al. 2010) have spectroscopic redshifts of ~ 2.23 . For the study of the Ly α luminosity functions in Section 4, we include these $z \sim 2.23$ broad-line AGNs and reject all the other AGNs. But for the study of star formation properties of LAEs, all broad-line AGNs are removed. The other possible contamination sources are Lyman-Break Galaxies (LBGs) at $z \sim 3$. At $z \sim 3$, both the narrowband and broad B band sample the continuum at rest-frame wavelength longer than 912Å while the U -band samples the rest-frame flux shorter than 912Å. The break makes interpolation between U and B band artificially low and NB-UB appears to be excessive. We simply use NB- B color to reject $z \sim 3$ LBGs. The reliability of this criterion was tested by LBGs selected by the classical LBG technique. Specifically, we apply the criteria proposed by Álvarez-Márquez et al. (2016) to select $z \sim 3$ LBGs in our COSMOS field using the COSMOS public archival catalogue and the criteria adopted by Hildebrandt et al. (2005) to select $z \sim 3$ LBGs in our ECDF-S field using the MUSYC public catalogue. As shown in Figure

5, LBGs mostly have $NB - B \geq 0$ and LAEs have $NB - B < 0$, although a minority of LBGs have $NB - B < 0$. A more strict criterion of $NB - B \geq -0.3$ would not change our results significantly. This criterion only identifies 5 $z \sim 3$ LBGs in COSMOS that were rejected from the sample. The final sample consists of 194 LAE candidates (including 4 AGNs) in COSMOS and 258 LAE candidates (including 2 AGNs) in ECDF-S, respectively.

Both EW and narrowband flux limit have selection effects in a narrowband-excess-selected LAE sample. Figure 6 shows that our sample does not include LAEs with low Ly α luminosity and high EW. This results from the narrowband detection limits. An LAE with low Ly α luminosity and high EW implies a low continuum, therefore its narrowband flux, i.e., the sum of the emission line flux and the continuum, is too low to be detected in the narrowband imaging (Guaita et al. 2010). From Figure 6, we also see that a larger number of faint LAEs were selected in ECDF-S than in COSMOS because of the deeper narrowband exposure in the ECDF-S field. The different selection criteria in EW employed by these two fields are also clearly seen in this figure. There are 31 LAEs with rest-frame EW between 20Å and 30Å in COSMOS, $\sim 16\%$ of the LAE sample in COSMOS. However, the inclusion of these LAEs compared to a selection criterion of $EW \geq 30\text{Å}$ does not change the number densities per luminosity bin significantly, due to the wide spread of these LAEs in the Ly α luminosity as shown in Figure 6. The changes are mostly within the 1σ Poisson noises.

4. LAE NUMBER COUNTS AND LY α LUMINOSITY FUNCTION

Measurement of galaxy number counts is a direct way of estimating depth of an imaging survey. We use Ly α magnitude/flux (with continuum subtracted, see equations (4) and (7)) to perform the analysis. The Ly α magnitude $m(\text{Ly}\alpha)$ is linked to the Ly α flux via the

⁶ <http://nedwww.ipac.caltech.edu/>

equation $m(\text{Ly}\alpha) = -2.5\log\left(\frac{F(\text{Ly}\alpha)\lambda_{\text{NB}}^2}{\Delta\lambda_{\text{NB}}\frac{\lambda_{\text{NB}}^2}{c}}\right) + m_0$, where c is the speed of light and m_0 is the zero-point of the AB magnitude system. The LAE number counts of the COSMOS and ECDF-S fields are listed in Table 2. In Figure 7, we plot our counts against those in previous narrow-band surveys with publicly available catalogs at similar redshifts. It shows that our counts reach a limiting flux density of $1.58 \times 10^{-17} \text{ erg s}^{-1} \text{ cm}^{-2}$. It is clear from Figure 7 that most surveys have consistent number counts up to $F(\text{Ly}\alpha) = 2.5 \times 10^{-17} \text{ erg s}^{-1} \text{ cm}^{-2}$, but at the faintest luminosity bin of $F(\text{Ly}\alpha) = 1.58 \times 10^{-17} \text{ erg s}^{-1} \text{ cm}^{-2}$, our survey has the highest counts comparing with previous surveys (Nilsson et al. 2009; Mawatari et al. 2012). Note that the narrowband imaging completeness corrected LAE number counts of the COSMOS and ECDF-S fields are different at the faintest end. This may be caused by different narrowband depths in the two fields and potential uncertainties associated with the large completeness correction in COSMOS at the faintest magnitude bin, as shown in Figure 6 and Figure 3 respectively.

With the deep LAE sample, we estimated Ly α luminosity function with the $< 1/V_{\text{max}} >$ method (Shimasaku et al. 2006; Ouchi et al. 2008; Gronwall et al. 2007; Hu et al. 2010; Konno et al. 2016). For a boxcar shape narrowband filter, it would be straightforward to derive the luminosity function by simply dividing the observed incompleteness-corrected number counts by their effective volume, i.e., the classical method (e.g., Shimasaku et al. 2006; Ouchi et al. 2008). However, in reality narrowband filter transmission curve does not have a boxcar shape, and the classical method suffers from some uncertainties, as noted by Ouchi et al. (2008). Ouchi et al. (2008) showed that these uncertainties are not important and/or cancel each other, but this may not apply to our samples due to the different filter shapes and survey properties. Unfortunately,

the sample sizes and the narrow coverage in Ly α luminosity do not allow us to perform a sophisticated simulation like Ouchi et al. (2008). So we assume the potential uncertainties caused by our non-boxcar filter profile cancel each other too.

Under the assumption that the redshift range corresponds to the FWHM of the narrow-band filter, the effective co-moving volumes probed by our narrowband surveys for COSMOS and ECDF-S fields are $1.16 \times 10^5 \text{ Mpc}^3$ and $1.18 \times 10^5 \text{ Mpc}^3$, respectively. The derived Ly α luminosity functions are provided in Table 3 and shown in Figure 8. The completeness at $L(\text{Ly}\alpha) < 10^{41.8} \text{ erg s}^{-1}$ is lower than 20%. We do not use LAEs below $10^{41.8} \text{ erg s}^{-1}$ in the estimation of the luminosity functions. The errors include uncertainties from both Poisson noise (Gehrels 1986) and cosmic variance. Following the method in Konno et al. (2016), the cosmic variance uncertainty is obtained from the bias factor of our LAEs derived in Section 5.3 and the dark matter density fluctuation in a sphere with a radius of $\sim 30 \text{ Mpc}$ (corresponding to our survey volume) at redshift 2.23. For both fields, the resultant cosmic variance uncertainty is 17.7%.

As can be seen in Figure 8, our Ly α luminosity functions of the two fields agree with each other and are generally consistent with those obtained in previous surveys (Hayes et al. 2010; Blanc et al. 2011; Cassata et al. 2011; Ciardullo et al. 2012; Konno et al. 2016). We specifically compare our results with the recent work by Konno et al. (2016) and Sobral et al. (2017). For a better comparison, apart from the best-fit luminosity functions, data points from Sobral et al. (2017) and data points with $L(\text{Ly}\alpha) > 10^{43} \text{ erg s}^{-1}$ from Konno et al. (2016) are also plotted in Figure 8. Both surveys observed an effective area of 1.43 deg^2 and probe a co-moving volume of $1.32 \times 10^6 \text{ Mpc}^3$ (Konno et al. 2016) and $7.3 \times 10^5 \text{ Mpc}^3$ (Sobral et al.

2017), respectively. The limiting Ly α luminosities are $10^{41.7}$ erg s $^{-1}$ for Konno et al. (2016) and $10^{42.3}$ erg s $^{-1}$ for Sobral et al. (2017), respectively. Although these surveys probe much larger areas and co-moving volumes than ours, we reach a comparable depth of Ly α luminosity limit of $10^{41.8}$ erg s $^{-1}$ with Konno et al. (2016) in the luminosity functions. Sobral et al. (2017) has made extensive comparisons with Konno et al. (2016). They showed that when the same EW threshold was used and no contaminants were removed, their Ly α luminosity function would be perfectly consistent with Konno et al. (2016). Even without matching the selection criteria, their results are claimed to be in good agreement with Konno et al. (2016) over most luminosities. Our luminosity functions roughly follow the trend of them, but the volume densities are systematically lower at $L(\text{Ly}\alpha) < 10^{43}$ erg s $^{-1}$. The possible causes for the differences are two-folds. One is the measurement of the total luminosity. We used aperture-corrected fluxes to probe the total flux while Konno et al. (2016) used MAG_AUTO and Sobral et al. (2017) used a larger aperture to measure the total flux. The other is the completeness correction. We used bright stars to evaluate the detection completeness and assumed effects caused by our non-boxcar filter profile cancel each other, similar to Konno et al. (2016). But Sobral et al. (2017) performed more corrections, including both selection completeness and filter profile biases.

To understand our systematically lower number densities than Konno et al. (2016) and Sobral et al. (2017), we derive Ly α luminosity functions using MAG_AUTO as a measure of the total flux and completeness curves built upon a reconstructed LAE narrowband image. The reconstructed LAE narrowband image is obtained by stacking the narrowband images of our LAEs. The approach used to construct the completeness curves is similar to that us-

ing bright stars in Section 2.4. The difference is that the reconstructed and flux-scaled LAE narrowband images are used as the input fake narrowband images and MAG_AUTO is used to measure the flux of the fake objects. The stacked LAE for each field has a FWHM of $\sim 0.7''$, slightly broader than the PSF. It is the requirement of the recovery (within 3σ) of the input MAG_AUTO that makes the detection completeness different from the ones using bright stars and aperture-corrected magnitudes, as shown in Figure 3. The resultant Ly α luminosity functions are added to Table 3 and shown in Figure 9. The luminosity functions based on aperture-corrected fluxes and completeness curves derived with stars are overplotted as gray open points for comparison. As can be seen, our results based on MAG_AUTO and completeness from the reconstructed LAE image agree well with the Ly α luminosity function of Sobral et al. (2017), although the number densities are still slightly lower than Konno et al. (2016). Virtually, the offsets between the Ly α luminosity functions based on our two methods are mostly within 1σ uncertainties as seen from Figure 9. The number densities based on the aperture-corrected fluxes and completeness derived using stars are systematically low though. The main contributor of the systematics comes from the completeness correction. This is especially the case for the faint part, as clearly shown in Figure 3. Therefore, we caution that systematics potentially introduced by different methods should be considered when Ly α luminosity functions from different studies are compared. Although number densities are affected by completeness corrections, the slope of our Ly α luminosity functions at the faint end is consistent with Konno et al. (2016) and Sobral et al. (2017), regardless the use of measures of total fluxes and completeness curves.

Regarding to the bright end ($L(\text{Ly}\alpha) > 10^{43}$ erg s $^{-1}$) of the luminosity functions, our

results are consistent with Konno et al. (2016) but show higher volume densities than Sobral et al. (2017), as shown in both Figure 8 and Figure 9. The use of MAG_AUTO and completeness curves based on the reconstructed LAE image does not change our bright-end luminosity functions dramatically. Sobral et al. (2017) claimed that the higher volume densities at the bright end in Konno et al. (2016) are caused by contaminations from non-LAE AGNs. Our AGNs are spectroscopically confirmed $z \sim 2.23$ LAEs, so our higher volume densities than Sobral et al. (2017) are real. But we note that the bright-end luminosity functions suffer from small number statistics. There are typically 1-2 objects in each bin. Virtually, the figures show that the bright-end difference between our data points and the results in Sobral et al. (2017) is mostly within 1σ errors. Furthermore, the cosmic variance uncertainties are probably underestimated since AGNs have much larger bias factor than our LAEs (Allevato et al. 2011). The actual error bars should be even larger, which would lead to a conclusion that the bright end of our Ly α luminosity functions is consistent with that of Sobral et al. (2017) within 1σ uncertainties.

5. LAES AS LOW MASS GALAXIES AT $Z \sim 2.23$

The universe was in a critical epoch at $z \sim 2$ when SFR density reached the highest. Most studies at this redshift focused on massive galaxies. Low mass galaxies are also important in constraining galaxy formation models. Yet it is quite challenging to identify low-mass galaxies at high redshifts. The narrowband technique provides an effective way to detect LAEs with very low stellar masses at high redshifts. However, only a small fraction of them are detected in longer wavelength bands (e.g., Nilsson et al. 2011), making it hard to estimate their stellar population parameters. We specifically chose both COSMOS and ECDF-S

fields where deep ancillary photometry data, especially deep *Spitzer*/IRAC observations, are available. Therefore we are able to study the properties of low-mass galaxies at $z \sim 2$ by investigating their stellar population, star formation property and dark matter halo mass.

5.1. *Stellar Population and Stellar Mass Function*

The *Spitzer* Extended Deep Survey (SEDS; Ashby et al. 2013) reaches limiting flux densities of sub micro-Jansky in $3.6 \mu\text{m}$ and $4.5 \mu\text{m}$ for COSMOS and ECDF-S, providing critical constraints on stellar mass measurements for faint LAEs in these two fields. Out of the 446 sample non-AGN LAEs, 130 ($\sim 29\%$) were detected in the SEDS imaging, which include 96 ($\sim 38\%$) LAEs in the ECDF-S field and 34 ($\sim 18\%$) LAEs in the COSMOS field. The different SEDS detection fractions in COSMOS and ECDF-S are due to the fact that SEDS only covers a part ($10' \times 60'$ strip) of our narrowband observed area in COSMOS. For the 130 IRAC-detected LAEs, we estimated their stellar masses using the SED fitting software FAST (Kriek et al. 2009). Multi-wavelength SEDs were constructed as follows: The optical and NIR data are retrieved from MUSYC (Cardamone et al. 2010), GEMS (Rix et al. 2004), Taiwan ECDFS Near-Infrared Survey (TENIS; Hsieh et al. 2012), COSMOS (Capak et al. 2007) and SEDS (Ashby et al. 2013). Specifically, MUSYC U , B bands, GEMS F606W, F850LP bands, TENIS J , K_s bands and SEDS $3.6 \mu\text{m}$, $4.5 \mu\text{m}$ are used for the ECDF-S field, while u^* , B_J , V_J , r^+ , i^+ , z^+ , J , K_s bands from the COSMOS photometry catalog and SEDS $3.6 \mu\text{m}$, $4.5 \mu\text{m}$ are used for the COSMOS field⁷. The stellar population synthesis models of Bruzual & Charlot (2003) was

⁷ For some LAEs, there are no photometric data available in a few required wavebands. But the remaining wavebands data, especially the crucial MIR bands

adopted, assuming a Salpeter IMF, an exponentially declining star formation history and a stellar metallicity of $0.2Z_{\odot}$. For dust attenuation modeling, the Calzetti dust extinction law (Calzetti et al. 2000) was used. Figure 10 shows examples of our SED fitting for two IRAC-detected LAEs. We note that $H\alpha$ emission contributes to the K_s band flux densities that would potentially bias the stellar mass estimates. So we performed SED fitting without using K_s band data and found that the stellar masses do not change much. In other words, no systematic biases were introduced by including K_s band in the SED fitting. The stellar masses were mainly constrained by the SEDS MIR data.

Our SED fitting results show that the stellar masses for most IRAC-detected LAEs are in the range of $8 < \log(M_{\star}/M_{\odot}) < 10$, but there do exist massive LAEs with stellar mass larger than $10^{10}M_{\odot}$, even more massive than $10^{11}M_{\odot}$. On the other hand, for IRAC-undetected LAEs, we use stacking analysis to derive a median SED. As mentioned above, SEDS only covers a part of our narrowband imaging survey area for COSMOS. To achieve high signal-to-noise ratio, we only used IRAC-undetected LAEs in ECDF-S for the stacking analysis. The stacked IRAC $3.6\mu\text{m}$ and $4.5\mu\text{m}$ magnitudes for the IRAC-undetected LAEs are 26.93 ± 0.09 and 27.02 ± 0.14 mag, respectively, which are similar to the stacking result for LAEs at $z \sim 3.1$ (Lai et al. 2008). Figure 11 presents the median-stacked SED along with the best-fit, which yields a stellar mass of $\log(M_{\star}/M_{\odot}) = 7.97^{+0.05}_{-0.07}$ and dust extinction of $A_v = 0.12^{+0.25}_{-0.08}$ mag. This is among the lowest mean stellar mass compared to the LAE samples in previous studies (Vargas et al. 2014; Hagen et al. 2014, 2016). In Figure 11, we note that the B band photometry is far above

provide reasonable constraints on the SED shapes and hence the stellar masses.

the best-fit but we cannot figure out the reason for this unreasonably high flux. Fortunately, the stellar mass and dust attenuation are not affected by this photometric data point. If B band photometry is not included in the SED fitting, the results only change within 1σ errors.

Although LAEs may just be one of the high-redshift galaxy populations with $\log(M_{\star}/M_{\odot}) \sim 8$, there are few studies on galaxies with such a low stellar mass at $z \sim 2$ besides LAEs, thus poor constraints on the low-mass end of the stellar mass function. With the estimation of a median stellar mass of $\sim 10^8M_{\odot}$ from the IRAC-undetected LAEs, we can have a rough estimation of their number density. This was simply done by dividing the number of IRAC-undetected LAEs by the product of the effective co-moving volume and the stellar mass range, without any corrections. Since stellar mass cannot be derived for IRAC-undetected LAEs individually, the stellar mass range cannot be estimated in the normal way. Instead, we estimated the stellar mass range via the star formation rate range. The stellar mass range in log-space is equal to the logarithmic star formation rate range under the assumption that the specific SFRs (i.e., SFR/M_{\star}) of these IRAC-undetected LAEs are the same. We estimated the star formation rate range covered by the IRAC-undetected LAEs using the rest-frame UV-derived SFRs (c.f. Section 5.2) of these LAEs and obtained the number density of $\log(\Phi/\text{Mpc}^{-3}\text{dex}^{-1}) = -3.0$ at $\log(M_{\star}/M_{\odot}) = 8$. We note that the number density derived this way suffers from large uncertainties introduced by the sample incompleteness and the assumption made in deriving the stellar mass range. It is probably a lower limit of the real number density considering the sample incompleteness. But it is still worth examining its position on the stellar mass function diagram given its low stellar mass.

Figure 12 shows the derived number density of our IRAC-undetected LAEs in the stellar mass function diagram, in comparison with the existing stellar mass functions at redshift $z \sim 2$ (Reddy & Steidel 2009; Santini et al. 2012; Ilbert et al. 2013; Muzzin et al. 2013; Tomczak et al. 2014; Mortlock et al. 2015). As can be seen from Figure 12, the only number density measurement to $\log(M_*/M_\odot) = 8$ are based on the BX redshift sample (Reddy & Steidel 2009) and are much lower than ours. All photometric redshift samples at $z \sim 2$ are not deep enough to reach this mass limit. However, these stellar mass functions at $\log(M_*/M_\odot) = 9.5$ are already a factor of $\sim 4 - 5$ higher than our LAE at $\log(M_*/M_\odot) = 8$. Therefore, our estimation provides a lower limit for the mass function at this mass limit.

If the extrapolation of the previous stellar mass functions to the low-mass end traces the real stellar mass function, we must answer the question: which types of galaxies compose of the low-mass galaxy population? Besides the LAEs, possible populations are galaxies with large amount of dust, galaxies that have been quenched or genuine star-forming galaxies with dust/gas geometries and orientations preventing Ly α photons escaping from the galaxies. However, dusty galaxies tend to be massive (e.g., Whitaker et al. 2012, 2014), and thus it is impossible for them to be a major population at the low-mass end of the stellar mass function. On the other hand, it is also unlikely that the quenched galaxies dominate the low-mass end of stellar mass function (e.g., Tomczak et al. 2014). The most possible missing low-mass galaxies are star-forming galaxies with interstellar medium (ISM) geometries and orientations against the escape of Ly α photons. It is difficult to identify the fraction of such galaxies at the moment because of their faint continua. Future deep observations in NIR/MIR by the James

Webb Space Telescope (JWST) may shed light on this.

5.2. Star Formation Properties

The SFMS relation and its extrapolation towards low-mass end have been widely used to characterize the star formation mode of LAEs. However, agreement has not been reached on the locations of LAEs relative to the SFMS relation (Guaita et al. 2013; Hagen et al. 2014; Vargas et al. 2014; Oteo et al. 2015; Hagen et al. 2016; Shimakawa et al. 2017; Kusakabe et al. 2018). Differences in the narrowband survey depths and the adoption of extinction curves may be responsible for the discrepancy (Shimakawa et al. 2017; Kusakabe et al. 2018). Given that our survey is among the deepest narrowband surveys and our sample is the largest LAEs sample with individual stellar mass measurements, it is worth revisiting the SFMS relation based on our LAEs sample.

The rest-frame FUV luminosity is the most commonly used SFR tracer at high redshifts. We calculated the rest-frame FUV luminosities for our sample LAEs from the observed *B*-band flux densities. Then the FUV luminosities were converted to SFRs using a conversion factor derived using STARBURST99 version 7.0.1 (Leitherer et al. 1999, 2010, 2014; Vázquez & Leitherer 2005) synthesis models for a constant star-forming population with age of 100 Myr and $0.2 Z_\odot$ stellar metallicity:

$$\text{SFR}(M_\odot \text{ yr}^{-1}) = 1.35 \times 10^{-28} L_\nu (\text{erg s}^{-1} \text{ Hz}^{-1}). \tag{8}$$

Dust attenuations were not accounted for in the SFRs derived here. The dust-uncorrected SFRs for IRAC-detected LAEs in both COSMOS and ECDF-S are in a range of $0.1 < \text{SFR} < 10 M_\odot \text{ yr}^{-1}$, while for the LAEs without IRAC detections, the median SFR is $\log(\text{SFR}/M_\odot \text{ yr}^{-1}) = -0.14$ with a rms scatter of 0.35 dex. In addition, six massive LAEs with stellar masses about $10^{11} M_\odot$ in the two fields are detected at

MIPS $24\mu\text{m}$ or even at *Herschel* FIR bands. We calculated their SFRs using the MIPS $24\mu\text{m}$ flux densities (Rieke et al. 2009), which are so high that they are qualified as Luminous Infrared Galaxies (LIRGs) or even Ultra-Luminous Infrared Galaxies (ULIRGs). Considering the large PSFs of the MIR/FIR images, we inspected the *Spitzer*/IRAC $3.6\mu\text{m}$ and MIPS $24\mu\text{m}$ images for these six LAEs and confirmed that their high MIR emissions are not from contaminations by neighboring bright objects.

The left panel of Figure 13 shows the locations of our sample LAEs on the dust-uncorrected SFR versus stellar mass diagram. The red solid circles and blue solid triangles represent LAEs in the COSMOS and ECDF-S fields, respectively, while the large red and blue inverted triangles denote the MIR/FIR-detected LAEs in the respective fields. For comparison, we also plot $z \sim 2$ BzK-selected galaxies with dust-corrected SFRs (Rodighiero et al. 2011), $\text{H}\alpha$ emitters with dust-corrected SFRs (HAEs; An et al. 2014) and the 50 LAEs in Shimakawa et al. (2017) with dust-uncorrected SFRs. The widely used $z \sim 2$ SFMS relations from Daddi et al. (2007) and Shivaiei et al. (2015) are overplotted in this figure. It is clear from the left panel of Figure 13 that the majority of our IRAC-detected LAEs and the stacked IRAC-undetected LAEs are located on the SFMS relations or their extrapolations towards low stellar mass end, within 1σ scatters (0.3 dex). In addition, the six MIR/FIR-detected massive LAEs with high SFRs are also on the SFMS relation and mix with the BzK-selected galaxies. The left panel of Figure 13 also shows that our 130 IRAC-detected LAEs are well mixed with the 50 LAEs of Shimakawa et al. (2017). Nevertheless, we note that as the stellar mass increases, the fraction of LAEs below SFMS also increases. Especially, as the stellar mass is larger than a few times

$10^9 M_\odot$, almost all LAEs are below the SFMS line. It may imply that more massive LAEs tend to be dustier and dust attenuation corrections are necessary for LAEs.

Currently, dust attenuations for LAEs are derived from SED fitting or from the UV slope β ($f_\lambda \propto \lambda^\beta$). Given that the color excess $E(B-V)$ derived via SED fitting is affected by the stellar mass (Shivaiei et al. 2015), we estimate $E(B-V)$ from the UV slope β in this work. The UV slope β could be determined reasonably well if several wavebands data covering the rest-frame 1300–2600 Å are available. This wavelength range corresponds to the B , V , R and I bands for objects at $z \sim 2.23$. For the 34 IRAC-detected LAEs in the COSMOS field, 33 are in the COSMOS public catalog and have deep B_J , V_J , r^+ , i^+ bands measurements, while for the ECDF-S field, only 58 out of 96 IRAC-detected LAEs have MUSYC B , V , R and I photometry. The six MIR/FIR-detected LAEs are included in the subsample with B , V , R and I bands photometry. We obtained β by fitting a power-law to the four bands flux densities via chi-square minimization⁸. After excluding the six MIR/FIR-detected LAEs and LAEs with unreliable β measurements, we were left with 27 LAEs in COSMOS and 51 LAEs in ECDF-S with reliable β . The uncertainties in β vary from 2% to 49% and have been incorporated into the total error budget in dust-corrected SFRs subsequently. The Calzetti extinction law (Calzetti et al. 2000) was then used to calculate $E(B-V)$ from β under the assumption that the intrinsic UV slope β_0 is -2.23 (Meurer et al. 1999). For objects with $\beta < -2.23$, zero dust extinctions were assumed. Figure 14 shows the

⁸ For four objects in COSMOS and three objects in ECDF-S, their UV continuum are suspicious and the four wavebands power-law fitting is with large errors in the best-fit values, i.e. larger than 50%. Thus these objects were excluded in the dust-correction related analysis.

distributions of β with a median of -1.8 for the 78 IRAC-detected LAEs with B , V , R and I measurements. As can be seen, there are 15 LAEs with $\beta < -2.23$ and hence zero dust extinctions. Figure 14 also reveals a broad distribution in β for LAEs in both fields, which leads to a wide range of $E(B-V)$ varying from 0 to 0.3 mag, with a median value of 0.1 mag. Using the $E(B-V)$, we obtained the dust-corrected SFRs for the 78 IRAC-detected LAEs spanning a range of $1 < \text{SFR} < 100 M_{\odot} \text{yr}^{-1}$. It should be noted that due to the lack of B , V , R and I photometry, dust corrections were not performed for 39 IRAC-detected LAEs. The 39 LAEs have lower dust-uncorrected SFRs than most of the LAEs that have B , V , R and I measurements.

The right panel of Figure 13 presents the 84 LAEs with dust-corrected SFRs, including the six MIR/FIR-detected LAEs whose SFRs were calculated from $24 \mu\text{m}$ fluxes and the 15 LAEs with zero dust extinctions. The LAEs in Shimakawa et al. (2017) are also plotted with dust-corrected SFRs. The symbols are the same as those in the left panel of Figure 13. Note that we also plot the 39 LAEs without dust corrections for their SFRs in the figure by solid gray circles or triangles. As shown in the right panel of Figure 13, most LAEs with dust-corrected SFRs are located along the SFMS within 1σ scatter, although a small fraction of LAEs are located above the SFMS, indicating that they are in active star formation mode. As for the stacked IRAC-undetected LAEs, we do not perform dust corrections because they have minor dust attenuation as derived from the SED fitting. It is obvious that these low-mass LAEs sit on the low-mass extrapolations of the SFMS. On the other hand, the LAEs with stellar mass larger than $10^{10} M_{\odot}$, along with the MIR/FIR-detected (U)LIRGs-like LAEs, are on the SFMS as well. In summary, LAEs are heterogeneous populations that have stellar

masses and SFRs covering more than three orders of magnitude, i.e., $8 < \log(M_{\star}/M_{\odot}) < 11.5$, $1 < \text{SFR} < 2000 M_{\odot} \text{yr}^{-1}$ and suffer from dust extinctions spanning a wide range. However, LAEs are mostly low-mass star-forming galaxies and they follow the SFMS relations defined by massive normal star-forming galaxies and their extrapolations to the low mass regime. This suggests that they are normal star-forming galaxies, instead of a special galaxy population in terms of star formation modes. It is unusual that an LAE is massive and MIR/FIR luminous, since even a small amount of dust could stop Ly α photons from escaping the galaxy. Such dusty, massive LAEs may have special dust/gas geometries favoring the escape of Ly α photons, as suggested by studies on Ly α and optical emission line profiles from local ULIRGs (Martin et al. 2015).

In the literature, different conclusions have been drawn on the relations of LAEs with respect to the SFMS. Survey depths and use of extinction curves have been proposed to be the causes. Since Shimakawa et al. (2017) have comparable narrowband survey depth with ours, we overplotted their LAEs with and without dust attenuation corrections in SFRs in the left and right panels of Figure 13 for comparison. We can see from the left panel of Figure 13 that the two LAE samples cover almost the same range in both the stellar mass and the dust-uncorrected SFR. Virtually, the two sample LAEs are mixed together in the dust-uncorrected SFR versus stellar mass diagram. On the other hand, the right panel of Figure 13 shows that the LAEs from the two samples are mostly mixed well except a lack of our LAEs in the low SFRs part, which is caused by the absence of broad B , V , R and I bands photometry for low SFR objects. Furthermore, we inspected Figure 10 of Hagen et al. (2014) who studied LAEs with high Ly α luminosities ($L(\text{Ly}\alpha) > 10^{43} \text{erg s}^{-1}$), at which there are

almost no LAEs below the SFMS line. In comparison with the right panel of Figure 13 in this work, the absence of LAEs below the SFMS in Hagen et al. (2014) seems to be caused by the selection effect that relatively shallow narrowband surveys leave out galaxies with lower SFRs, as pointed out by Oyarzún et al. (2017). Regarding to the adoption of extinction laws, both Shimakawa et al. (2017) and this work use the Calzetti extinction curve and find that the LAEs are not significantly above the SFMS relations in the dust-corrected SFR versus stellar mass diagram. Therefore, it seems that it is not a necessity to employ a different extinction law.

5.3. Dark Matter Halo Mass

In the Λ CDM paradigm, galaxies form in dark matter halos, and galaxy evolution is closely linked to its hosting dark matter halo mass. In this subsection, we derive the dark matter halo mass for our LAEs. The bias factor and dark matter halo mass of our LAEs sample were estimated via clustering analysis following Guaita et al. (2010) and Kusakabe et al. (2018). First, we calculated the angular two-point correlation function using the Landy-Szalay estimator (Landy & Szalay 1993):

$$w(\theta) = \frac{DD(\theta) - 2DR(\theta) + RR(\theta)}{RR(\theta)}, \quad (9)$$

where DD, DR and RR are the normalized counts for data-data, data-random, and random-random pairs, respectively. We generated a random sample that is 200 times the LAE sample size with the same geometry. A power law form $w(\theta) = A\theta^{-\beta}$ was assumed for the angular correlation function. However, due to the limited size of the survey area, the observed angular correlation function is actually $w(\theta) - AC = A(\theta^{-\beta} - C)$, where AC is the integral constraint. By performing a Monte Carlo integration, we can first estimate C (e.g., Roche et al. 1999) and then fit

$A(\theta^{-\beta} - C)$ to the data. The clustering amplitude A was thus obtained from the fitting by further fixing β to 0.8 following the literature (e.g., Guaita et al. 2010; Matsuoka et al. 2011; Coupon et al. 2012). Note that we only used a selected range of θ ($50'' \lesssim \theta \lesssim 600''$) during the fitting, in order to avoid the influence of the one-halo term at small scales ($\theta < 50''$) and sampling noise at large scales. The best-fit values of A and the integral constraint are $9.5 \pm 2.2 \text{ arcsec}^{0.8}$ and 0.06, respectively. The angular two-point correlation function, along with the best-fit curve of our LAEs are shown in Figure 15.

Corresponding to the power law form of $w(\theta)$, the spatial correlation function has the form of $\xi(r) = (r/r_0)^{-(\beta+1)}$. Assuming a Gaussian distribution of the LAE redshifts within our narrowband window, we obtained the real space correlation length according to Simon (2007), which is 3.66 ± 0.47 Mpc. Then we calculated the bias factor of LAEs by $b = \sqrt{\frac{\xi(r)}{\xi_{\text{DM}}(r)}}$, where $\xi(r)$ and $\xi_{\text{DM}}(r)$ are the correlation function of LAEs and the underlying dark matter in the linear theory, respectively. Here r is chosen to be $8h^{-1}$ Mpc, following Ouchi et al. (2003) and Kusakabe et al. (2018). The resultant bias factor is 1.31 ± 0.15 . Finally, the halo mass M_h was obtained via the relation between bias factor and the peak height in the linear density field $\nu = \delta_c/\sigma(M_h, z)$ (Tinker et al. 2010), where $\delta_c = 1.686$ is the critical overdensity for dark matter collapse and $\sigma(M_h, z)$ is the rms fluctuation in a sphere that encloses mass M_h on average at present time, extrapolated to redshift z with the linear theory. The bias factor derived above corresponds to a mean dark matter halo mass of $\log(M_h/M_\odot) = 10.8_{-0.42}^{+0.26}$. Note that the errors reported here do not account for cosmic variance. Since our survey area (COSMOS and ECDF-S fields) is just $\sim 0.34 \text{ deg}^2$, cosmic variance should be important, as discussed by Kusakabe et al. (2018). According to

the scaling relation in Kusakabe et al. (2018), we estimated an uncertainty of $\sim 46\%$ due to cosmic variance in the bias factor, resulting in a bias factor of 1.31 ± 0.34 and halo mass of $\log(M_h/M_\odot) = 10.8_{-1.1}^{+0.56}$. Most recently, based on a large sample (1937 LAEs) of $z \sim 2.2$ LAEs with $NB387_{\text{tot}} \leq 25.5$ mag in four survey fields covering a total area of $\simeq 1$ deg 2 , Kusakabe et al. (2018) obtained a bias factor of $1.22_{-0.26}^{+0.23}$ and halo mass of $\log(M_h/M_\odot) = 10.6_{-0.9}^{+0.5}$. Accordingly, they predicted that in the local universe their LAEs would be typically hosted by dark matter halos with mass comparable to that of the Large Magellanic Cloud (LMC). The bias factor and halo mass based on our 446 LAEs are consistent with those of Kusakabe et al. (2018) within 1σ , although the errors in our analysis are larger due to the smaller survey area. Therefore, the dark matter halo hosting our LAEs may similarly evolve into a LMC-like halo at $z = 0$.

6. SUMMARY

We have conducted deep narrowband surveys for the COSMOS and ECDF-S fields to search for Ly α emitters (LAEs) at redshift $z = 2.23 \pm 0.03$ using our customized narrowband filter $N3928 \text{ \AA}$ at Megacam/Magellan II telescope. Our observations reached a 5σ limiting magnitudes in a $3''$ diameter aperture of ~ 26 mag and a seeing FWHM of $0''.6$. Using archival broad U and B bands images as a measure of the underlying continuum, we selected 194 (including 4 AGNs) and 258 (including 2 AGNs) LAEs over the 602 arcmin 2 and 613 arcmin 2 survey areas on the COSMOS and ECDF-S fields, respectively. Our LAEs sample provides reliable measurements of the Ly α luminosity function over the Ly α luminosity range of $10^{41.8} - 10^{42.8}$ erg s $^{-1}$. Within this luminosity range, the Ly α luminosity functions of the COSMOS and ECDF-S fields are in a good agreement with each other. The overall shapes of our Ly α luminosity functions are consistent with

that of Konno et al. (2016) and Sobral et al. (2017) based on larger area (1.43 deg 2) Ly α surveys at similar redshifts. Thus our Ly α luminosity functions lend further support to the steep faint-end slope.

The existing multi-wavelength data from the rest-frame UV to the IR, especially the deep *Spitzer*/IRAC MIR data, allow us to explore the stellar populations and star formation properties of LAEs. The *Spitzer* Extended Deep Survey (SEDS) provides important constraints on the stellar mass estimates. For 29% of our LAEs that were detected by IRAC at $3.6 \mu\text{m}$ or $4.5 \mu\text{m}$, their stellar masses are in the range of $8 < \log(M_\star/M_\odot) < 11.5$. On the other hand, the SED fitting to the stacked SED of the IRAC-undetected LAEs indicates a stellar mass of $\log(M_\star/M_\odot) = 7.97_{-0.07}^{+0.05}$ and dust extinction of $A_v = 0.12_{-0.08}^{+0.25}$ mag. Based on the measurement of the median stellar mass for the IRAC-undetected LAEs, we roughly estimate their mean number density as $\log(\Phi/\text{Mpc}^{-3}\text{dex}^{-1}) = -3.0$ at $\log(M_\star/M_\odot)=8$. Although it is a lower limit and much smaller than the extrapolation of the existing stellar mass functions, it serves as an important observational constraint at such low-mass regime.

Rest-frame FUV luminosities calculated from the observed B -band flux densities were used to derive SFRs. The dust attenuations were estimated from the UV slope β , based on public B , V , R and I bands photometry. The dust-corrected SFRs of our LAEs cover a range of $1 < \text{SFR} < 100 M_\odot \text{ yr}^{-1}$, with six *Spitzer*/MIPS $24 \mu\text{m}$ or even *Herschel* FIR detected LAEs having SFRs up to $2000 M_\odot \text{ yr}^{-1}$. Although LAEs are heterogeneous populations that have stellar mass and SFR covering more than three orders of magnitude, i.e. $8 < \log(M_\star/M_\odot) < 11.5$, $1 < \text{SFR} < 2000 M_\odot \text{ yr}^{-1}$, they are mostly composed of low-mass galaxies and follow the star formation main sequence relations and their extrapolations to the low mass end. This indicates

that the star formation in most LAEs is taking place in a steady mode.

The two-point correlation function analysis for our LAEs sample yields a bias factor of 1.31 ± 0.34 and corresponding dark matter halo mass of $\log(M_h/M_\odot) = 10.8_{-1.1}^{+0.56}$, which is consistent with those of [Kusakabe et al. \(2018\)](#) based on a much larger sample and survey area.

We would like to thank the anonymous referee for very helpful comments and suggestions that improved the paper. We also thank Drs. Haruka Kusakabe, Hong Guo, Jun Pan, Jie Wang for helpful discussions. We acknowledge Dr. Giulia Rodighiero for kindly providing their data for BzK samples in the star formation main sequence diagram and Dr. Maureen Conroy for instructing us to run the TCL script “megawcs”. This work is supported by the National Key Research and Development Program of China (No. 2017YFA0402703) and the National Natural Science Foundation of China (NSFC, No. 11373027 and 11733002). X.Z.Z. thanks support from the NSFC (No. 11773076) and the Chinese Academy of Sciences (CAS) through a grant to the CAS South America Center for Astronomy (CASSACA) in Santiago, Chile. C.J. acknowledges support from the NSFC (No. 11773051), and the CAS Key Research Program of Frontier Sciences (No. QYZDB-SSW-SYS033). C.L. acknowledges the support by National Key Basic Research Programs of China (No. 2015CB857004) and National Key R&D Program of China (No. 2018YFA0404502), and the NSFC (No. 11173045, 11233005, 11325314, 11320101002). This research uses data obtained partially through the Telescope Access Program (TAP), which has been funded by the National Astronomical Observatories of China, the Chinese Academy of Sciences, and the Special Fund for Astronomy from the Ministry of Finance.

REFERENCES

- Acquaviva, V., Gawiser, E., & Guaita, L. 2011, *ApJ*, 737, 47
- Allevato, V., Finoguenov, A., Cappelluti, N., et al. 2011, *ApJ*, 736, 99
- Álvarez-Márquez, J., Burgarella, D., Heinis, S., et al. 2016, *A&A*, 587, A122
- An, F. X., Zheng, X. Z., Hao, C.-N., Huang, J.-S., & Xia, X.-Y. 2017, *ApJ*, 835, 116
- An, F. X., Zheng, X. Z., Wang, W.-H., et al. 2014, *ApJ*, 784, 152
- Ashby, M. L. N., Willner, S. P., Fazio, G. G., et al. 2013, *ApJ*, 769, 80
- Bertin, E., & Arnouts, S. 1996, *A&AS*, 117, 393
- Bertin, E., Mellier, Y., Radovich, M., et al. 2002, *Astronomical Data Analysis Software and Systems XI*, ASP Conference Proceedings, 281, 228
- Blanc, G. A., Adams, J. J., Gebhardt, K., et al. 2011, *ApJ*, 736, 31
- Brinchmann, J., Charlot, S., White, S. D. M., et al. 2004, *MNRAS*, 351, 1151
- Brammer, G. B., Whitaker, K. E., van Dokkum, P. G., et al. 2011, *ApJ*, 739, 24
- Bruzual, G., & Charlot, S. 2003, *MNRAS*, 344, 1000
- Burkert, A., Förster Schreiber, N. M., Genzel, R., et al. 2016, *ApJ*, 826, 214
- Caldwell, J. A. R., McIntosh, D. H., Rix, H.-W., et al. 2008, *ApJS*, 174, 136-144
- Calzetti, D., Armus, L., Bohlin, R. C., et al. 2000, *ApJ*, 533, 682
- Capak, P., Aussel, H., Ajiki, M., et al. 2007, *ApJS*, 172, 99
- Cardamone, C. N., van Dokkum, P. G., Urry, C. M., et al. 2010, *ApJS*, 189, 270
- Cassata, P., Le Fèvre, O., Garilli, B., et al. 2011, *A&A*, 525, A143
- Ciardullo, R., Gronwall, C., Wolf, C., et al. 2012, *ApJ*, 744, 110
- Ciardullo, R., Zeimann, G. R., Gronwall, C., et al. 2014, *ApJ*, 796, 64
- Civano, F., Elvis, M., Brusa, M., et al. 2012, *ApJS*, 201, 30
- Coupon, J., Kilbinger, M., McCracken, H. J., et al. 2012, *A&A*, 542, A5
- Daddi, E., Dickinson, M., Morrison, G., et al. 2007, *ApJ*, 670, 156
- Drake, A. B., Garel, T., Wisotzki, L., et al. 2017, *A&A*, 608, A6
- Elbaz, D., Daddi, E., Le Borgne, D., et al. 2007, *A&A*, 468, 33
- Erb, D. K., Shapley, A. E., Pettini, M., et al. 2006, *ApJ*, 644, 813
- Fang, G., Kong, X., Chen, Y., & Lin, X. 2012, *ApJ*, 751, 109
- Finkelstein, S. L., Rhoads, J. E., Malhotra, S., & Grogin, N. 2009, *ApJ*, 691, 465
- Finkelstein, S. L., Rhoads, J. E., Malhotra, S., Grogin, N., & Wang, J. 2008, *ApJ*, 678, 655-668
- Finkelstein, S. L., Rhoads, J. E., Malhotra, S., Pirzkal, N., & Wang, J. 2007, *ApJ*, 660, 1023
- Förster Schreiber, N. M., Genzel, R., Bouché, N., et al. 2009, *ApJ*, 706, 1364
- Gawiser, E., Francke, H., Lai, K., et al. 2007, *ApJ*, 671, 278
- Gawiser, E., van Dokkum, P. G., Gronwall, C., et al. 2006, *ApJL*, 642, L13
- Geach, J. E., Smail, I., Best, P. N., et al. 2008, *MNRAS*, 388, 1473
- Gehrels, N. 1986, *ApJ*, 303, 336
- Grogin, N. A., Kocevski, D. D., Faber, S. M., et al. 2011, *ApJS*, 197, 35
- Gronwall, C., Ciardullo, R., Hickey, T., et al. 2007, *ApJ*, 667, 79
- Guaita, L., Francke, H., Gawiser, E., et al. 2013, *A&A*, 551, A93
- Guaita, L., Acquaviva, V., Padilla, N., et al. 2011, *ApJ*, 733, 114
- Guaita, L., Gawiser, E., Padilla, N., et al. 2010, *ApJ*, 714, 255
- Hagen, A., Zeimann, G. R., Behrens, C., et al. 2016, *ApJ*, 817, 79
- Hagen, A., Ciardullo, R., Gronwall, C., et al. 2014, *ApJ*, 786, 59
- Hathi, N. P., Le Fèvre, O., Ilbert, O., et al. 2016, *A&A*, 588, A26
- Hayes, M., Östlin, G., Schaerer, D., et al. 2010, *Nature*, 464, 562
- Hildebrandt, H., Bomans, D. J., Erben, T., et al. 2005, *A&A*, 441, 905
- Hsieh, B.-C., Wang, W.-H., Hsieh, C.-C., et al. 2012, *ApJS*, 203, 23
- Hu, E. M., Cowie, L. L., Barger, A. J., et al. 2010, *ApJ*, 725, 394

- Ilbert, O., Capak, P., Salvato, M., et al. 2009, *ApJ*, 690, 1236
- Ilbert, O., McCracken, H. J., Le Fèvre, O., et al. 2013, *A&A*, 556, A55
- Koekemoer, A. M., Faber, S. M., Ferguson, H. C., et al. 2011, *ApJS*, 197, 36
- Kriek, M., van Dokkum, P. G., Labbé, I., et al. 2009, *ApJ*, 700, 221
- Konno, A., Ouchi, M., Nakajima, K., et al. 2016, *ApJ*, 823, 20
- Konno, A., Ouchi, M., Ono, Y., et al. 2014, *ApJ*, 797, 16
- Kriek, M., Shapley, A. E., Reddy, N. A., et al. 2015, *ApJS*, 218, 15
- Kusakabe, H., Shimasaku, K., Ouchi, M., et al. 2018, *PASJ*, 70, 4
- Lai, K., Huang, J.-S., Fazio, G., et al. 2008, *ApJ*, 674, 70-74
- Landy, S. D., & Szalay, A. S. 1993, *ApJ*, 412, 64
- Lehmer, B. D., Brandt, W. N., Alexander, D. M., et al. 2005, *ApJS*, 161, 21
- Leitherer, C., Ekström, S., Meynet, G., et al. 2014, *ApJS*, 212, 14
- Leitherer, C., Ortiz Otálvaro, P. A., Bresolin, F., et al. 2010, *ApJS*, 189, 309
- Leitherer, C., Schaerer, D., Goldader, J. D., et al. 1999, *ApJS*, 123, 3
- Lilly, S. J., Le Fèvre, O., Renzini, A., et al. 2007, *ApJS*, 172, 70
- Luo, B., Bauer, F. E., Brandt, W. N., et al. 2008, *ApJS*, 179, 19-36
- Madau, P., & Dickinson, M. 2014, *ARA&A*, 52, 415
- Malhotra, S., & Rhoads, J. E. 2002, *ApJL*, 565, L71
- Martin, C. L., Dijkstra, M., Henry, A., et al. 2015, *ApJ*, 803, 6
- Matsuoka, Y., Masaki, S., Kawara, K., & Sugiyama, N. 2011, *MNRAS*, 410, 548
- Matthee, J., Sobral, D., Oteo, I., et al. 2016, *MNRAS*, 458, 449
- Mawatari, K., Yamada, T., Nakamura, Y., Hayashino, T., & Matsuda, Y. 2012, *ApJ*, 759, 133
- Meurer, G. R., Heckman, T. M., & Calzetti, D. 1999, *ApJ*, 521, 64
- Mortlock, A., Conselice, C. J., Hartley, W. G., et al. 2015, *MNRAS*, 447, 2
- Muzzin, A., Marchesini, D., Stefanon, M., et al. 2013, *ApJ*, 777, 18
- Nakajima, K., Ouchi, M., Shimasaku, K., et al. 2012, *ApJ*, 745, 12
- Nakajima, K., Ouchi, M., Shimasaku, K., et al. 2013, *ApJ*, 769, 3
- Nilsson, K. K., Östlin, G., Møller, P., et al. 2011, *A&A*, 529, A9
- Nilsson, K. K., Tapken, C., Møller, P., et al. 2009, *A&A*, 498, 13
- Nilsson, K. K., Møller, P., Möller, O., et al. 2007, *A&A*, 471, 71
- Ono, Y., Ouchi, M., Shimasaku, K., et al. 2010a, *ApJ*, 724, 1524
- Ono, Y., Ouchi, M., Shimasaku, K., et al. 2010b, *MNRAS*, 402, 1580
- Oteo, I., Bongiovanni, A., Pérez García, A. M., et al. 2012, *A&A*, 541, A65
- Oteo, I., Sobral, D., Ivison, R. J., et al. 2015, *MNRAS*, 452, 2018
- Ouchi, M., Shimasaku, K., Akiyama, M., et al. 2008, *ApJS*, 176, 301-330
- Ouchi, M., Shimasaku, K., Furusawa, H., et al. 2003, *ApJ*, 582, 60
- Oyarzún, G. A., Blanc, G. A., González, V., Mateo, M., & Bailey, J. I., III 2017, *ApJ*, 843, 133
- Pirzkal, N., Malhotra, S., Rhoads, J. E., & Xu, C. 2007, *ApJ*, 667, 49
- Rauch, M., Haehnelt, M., Bunker, A., et al. 2008, *ApJ*, 681, 856
- Reddy, N. A., & Steidel, C. C. 2009, *ApJ*, 692, 778
- Rieke, G. H., Alonso-Herrero, A., Weiner, B. J., et al. 2009, *ApJ*, 692, 556
- Rix, H.-W., Barden, M., Beckwith, S. V. W., et al. 2004, *ApJS*, 152, 163
- Roche, N., Eales, S. A., Hippelein, H., & Willott, C. J. 1999, *MNRAS*, 306, 538
- Rodighiero, G., Daddi, E., Baronchelli, I., et al. 2011, *ApJL*, 739, L40
- Salpeter, E. E. 1955, *ApJ*, 121, 161
- Salvato, M., Ilbert, O., Hasinger, G., et al. 2011, *ApJ*, 742, 61
- Santini, P., Fontana, A., Grazian, A., et al. 2012, *A&A*, 538, A33
- Scoville, N., Aussel, H., Brusa, M., et al. 2007, *ApJS*, 172, 1
- Shimakawa, R., Kodama, T., Shibuya, T., et al. 2017, *MNRAS*, 468, 1123
- Shimasaku, K., Kashikawa, N., Doi, M., et al. 2006, *PASJ*, 58, 313

- Shivaei, I., Reddy, N. A., Shapley, A. E., et al. 2015, *ApJ*, 815, 98
- Shivaei, I., Reddy, N. A., Shapley, A. E., et al. 2017, *ApJ*, 837, 157
- Silverman, J. D., Mainieri, V., Salvato, M., et al. 2010, *ApJS*, 191, 124
- Simon, P. 2007, *A&A*, 473, 711
- Skelton, R. E., Whitaker, K. E., Momcheva, I. G., et al. 2014, *ApJS*, 214, 24
- Sobral, D., Matthee, J., Best, P., et al. 2017, *MNRAS*, 466, 1242
- Sobral, D., Santos, S., Matthee, J., et al. 2018, *MNRAS*, 476, 4725
- Sobral, D., Smail, I., Best, P. N., et al. 2013, *MNRAS*, 428, 1128
- Steidel, C. C., Rudie, G. C., Strom, A. L., et al. 2014, *ApJ*, 795, 165
- Stiavelli, M., Scarlata, C., Panagia, N., et al. 2001, *ApJL*, 561, L37
- Taniguchi, Y., Kajisawa, M., Kobayashi, M. A. R., et al. 2015, *ApJL*, 809, L7
- Taylor, E. N., Franx, M., van Dokkum, P. G., et al. 2009, *ApJS*, 183, 295
- Tinker, J. L., Robertson, B. E., Kravtsov, A. V., et al. 2010, *ApJ*, 724, 878
- Tomczak, A. R., Quadri, R. F., Tran, K.-V. H., et al. 2014, *ApJ*, 783, 85
- Trainor, R. F., Strom, A. L., Steidel, C. C., & Rudie, G. C. 2016, *ApJ*, 832, 171
- Treister, E., Virani, S., Gawiser, E., et al. 2009, *ApJ*, 693, 1713
- Trump, J. R., Impey, C. D., Elvis, M., et al. 2009, *ApJ*, 696, 1195
- van Breukelen, C., Jarvis, M. J., & Venemans, B. P. 2005, *MNRAS*, 359, 895
- Vargas, C. J., Bish, H., Acquaviva, V., et al. 2014, *ApJ*, 783, 26
- Vázquez, G. A., & Leitherer, C. 2005, *ApJ*, 621, 695
- Virani, S. N., Treister, E., Urry, C. M., & Gawiser, E. 2006, *AJ*, 131, 2373
- Wang, J. X., Malhotra, S., & Rhoads, J. E. 2005, *ApJL*, 622, L77
- Whitaker, K. E., Franx, M., Leja, J., et al. 2014, *ApJ*, 795, 104
- Whitaker, K. E., van Dokkum, P. G., Brammer, G., & Franx, M. 2012, *ApJL*, 754, L29
- Williams, R. J., Quadri, R. F., Franx, M., van Dokkum, P., & Labbé, I. 2009, *ApJ*, 691, 1879
- Wuyts, E., Wisnioski, E., Fossati, M., et al. 2016, *ApJ*, 827, 74
- Zheng, Z.-Y., Malhotra, S., Rhoads, J. E., et al. 2016, *ApJS*, 226, 23
- Zheng, Z.-Y., Wang, J., Rhoads, J., et al. 2017, *ApJL*, 842, L22

Table 1. Narrowband observation parameters

| Field | RA ^a | DEC ^a | Total exposure (min) | PSF(FWHM) |
|--------|---|------------------|----------------------|-----------|
| ECDF-S | 3 ^h 32 ^m 26.0 ^s | -27°49'20" | 660 | 0.6" |
| COSMOS | 10 ^h 00 ^m 27.9 ^s | +2°12'03" | 600 | 0.6" |

^aThis indicates the center of the pointing.

Table 2. Number counts of LAEs

| m(Ly α) | dN/dm | (dN/dm) _{corr} |
|-----------------|--|--|
| (mag) | (10 ⁻² mag ⁻¹ arcmin ⁻²) | (10 ⁻² mag ⁻¹ arcmin ⁻²) |
| COSMOS | | |
| 22.25 | 0.33 ^{+0.76} _{-0.27} | 0.33 ^{+0.76} _{-0.27} |
| 22.75 | 1.00 ^{+0.97} _{-0.54} | 1.00 ^{+0.97} _{-0.54} |
| 23.25 | 0.33 ^{+0.76} _{-0.27} | 0.33 ^{+0.76} _{-0.27} |
| 23.75 | 1.99 ^{+1.19} _{-0.79} | 1.99 ^{+1.19} _{-0.79} |
| 24.25 | 1.99 ^{+1.19} _{-0.79} | 1.99 ^{+1.19} _{-0.79} |
| 24.75 | 8.97 ^{+2.08} _{-1.71} | 8.97 ^{+2.08} _{-1.71} |
| 25.25 | 13.96 ^{+2.50} _{-2.14} | 13.97 ^{+2.50} _{-2.14} |
| 25.75 | 18.27 ^{+2.81} _{-2.46} | 19.45 ^{+2.99} _{-2.62} |
| 26.25 | 14.95 ^{+2.58} _{-2.22} | 22.50 ^{+3.88} _{-3.34} |
| ECDF-S | | |
| 22.25 | ... | ... |
| 22.75 | 0.33 ^{+0.75} _{-0.27} | 0.33 ^{+0.75} _{-0.27} |
| 23.25 | 0.65 ^{+0.86} _{-0.42} | 0.65 ^{+0.86} _{-0.42} |
| 23.75 | 1.31 ^{+1.03} _{-0.62} | 1.31 ^{+1.03} _{-0.62} |
| 24.25 | 3.26 ^{+1.39} _{-1.01} | 3.26 ^{+1.39} _{-1.01} |
| 24.75 | 6.85 ^{+1.85} _{-1.49} | 6.85 ^{+1.85} _{-1.49} |
| 25.25 | 12.73 ^{+2.38} _{-2.03} | 12.73 ^{+2.38} _{-2.03} |
| 25.75 | 19.58 ^{+2.87} _{-2.52} | 19.96 ^{+2.93} _{-2.57} |
| 26.25 | 31.66 ^{+3.55} _{-3.21} | 39.24 ^{+4.40} _{-3.98} |

Table 3. Ly α Luminosity Function

| log [L(Ly α)] (erg s $^{-1}$) | Φ (COSMOS) ^a ($\frac{10^{-4}}{\text{Mpc}^3(\Delta\log L)}$) | Φ (ECDF-S) ^a ($\frac{10^{-4}}{\text{Mpc}^3(\Delta\log L)}$) | Φ (COSMOS) ^b ($\frac{10^{-4}}{\text{Mpc}^3(\Delta\log L)}$) | Φ (ECDF-S) ^b ($\frac{10^{-4}}{\text{Mpc}^3(\Delta\log L)}$) |
|---|--|--|--|--|
| 41.90 | 28.44 $^{+6.61}_{-6.28}$ | 33.05 $^{+7.28}_{-7.01}$ | 53.49 $^{+12.72}_{-12.01}$ | 49.11 $^{+10.82}_{-10.41}$ |
| 42.10 | 19.94 $^{+4.90}_{-4.59}$ | 19.95 $^{+4.87}_{-4.57}$ | 21.51 $^{+5.63}_{-5.19}$ | 19.88 $^{+5.08}_{-4.71}$ |
| 42.30 | 13.36 $^{+3.71}_{-3.36}$ | 12.29 $^{+3.49}_{-3.14}$ | 17.91 $^{+4.65}_{-4.29}$ | 11.88 $^{+3.46}_{-3.09}$ |
| 42.50 | 6.03 $^{+2.34}_{-1.92}$ | 6.36 $^{+2.38}_{-1.97}$ | 9.23 $^{+2.98}_{-2.58}$ | 8.50 $^{+2.80}_{-2.41}$ |
| 42.70 | 2.16 $^{+1.51}_{-1.01}$ | 1.27 $^{+1.26}_{-0.73}$ | 3.02 $^{+1.71}_{-1.24}$ | 1.27 $^{+1.26}_{-0.73}$ |
| 42.90 | 0.86 $^{+1.15}_{-0.58}$ | 1.69 $^{+1.37}_{-0.86}$ | 1.72 $^{+1.40}_{-0.88}$ | 1.69 $^{+1.37}_{-0.86}$ |
| 43.10 | 0.86 $^{+1.15}_{-0.58}$ | 0.42 $^{+0.98}_{-0.36}$ | 0.86 $^{+1.15}_{-0.58}$ | 1.27 $^{+1.26}_{-0.73}$ |
| 43.30 | 0.86 $^{+1.15}_{-0.58}$ | ... | 0.86 $^{+1.15}_{-0.58}$ | ... |
| 43.50 | ... | ... | 0.43 $^{+0.99}_{-0.36}$ | ... |

^aAperture-corrected fluxes and completeness curves based on bright stars are used.

^bFluxes represented by MAG_AUTO and completeness curves derived with the reconstructed narrowband image of our LAEs are used.

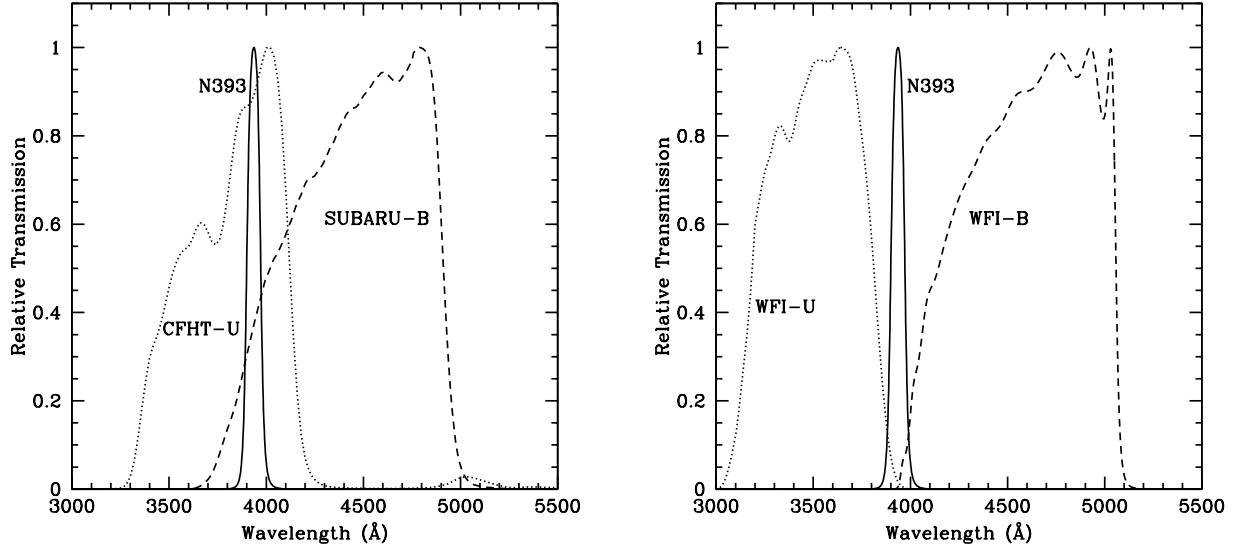


Figure 1. Filter transmission curves for COSMOS (left) and ECDF-S (right). The solid line represents our customized narrowband filter N393, while the dotted and dashed lines represent the broad U and B band filters.

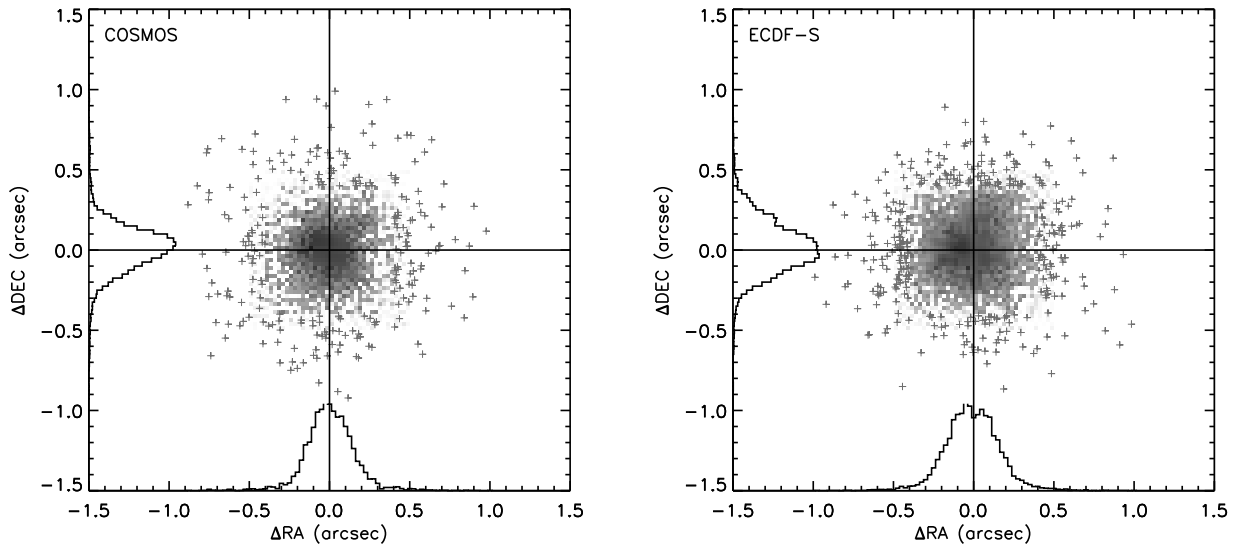


Figure 2. The offset in RA and DEC between our WCS calibration and the *HST*/ACS I -band catalog for the COSMOS (left) and the GEMS *HST*/ACS V -band catalog for the ECDF-S (right).

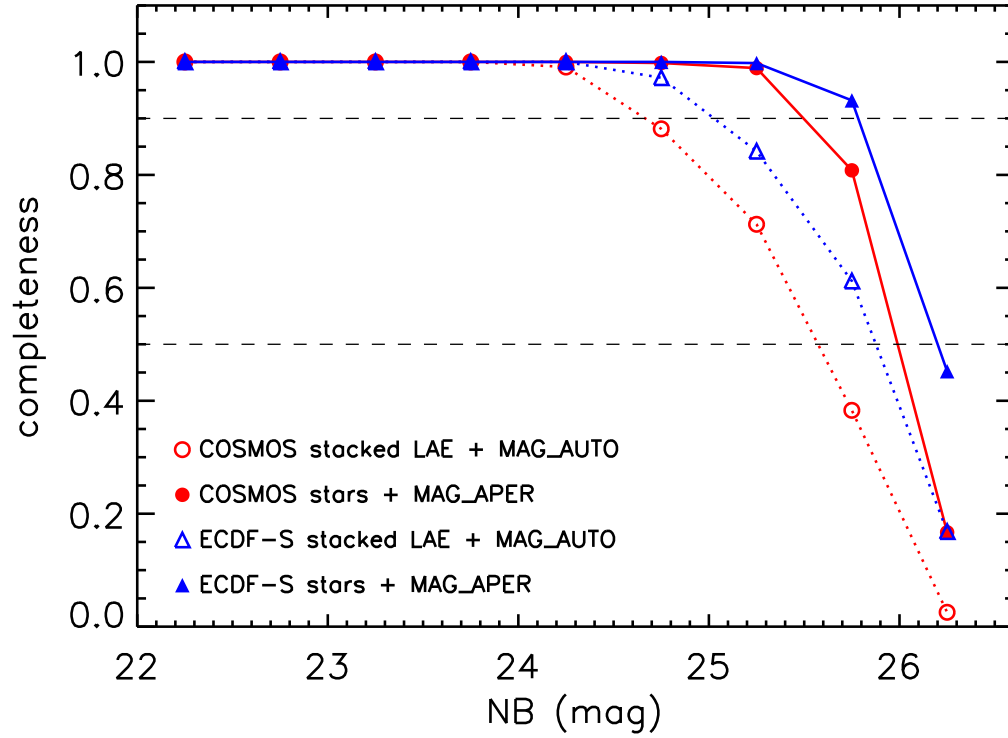


Figure 3. Completeness curves for COSMOS (red points) and ECDF-S (blue points). The solid points represent the completeness curves obtained using bright stars and aperture-corrected magnitudes, while the the open symbols indicate the completeness curves based on the stacked narrowband image of our LAEs and MAG_AUTO magnitudes.

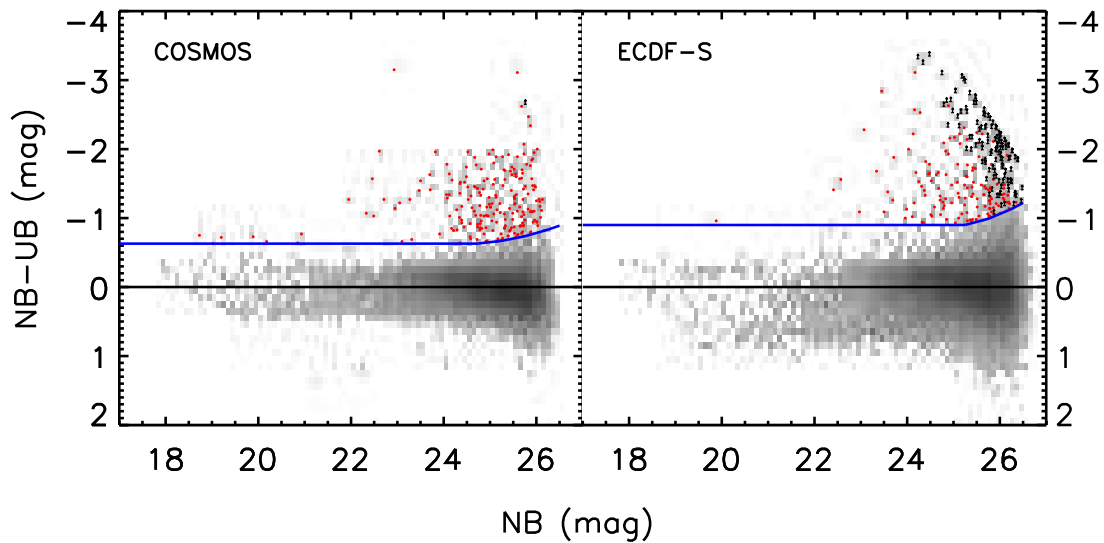


Figure 4. Narrowband color excess as a function of narrowband magnitude for the COSMOS (left) and ECDF-S (right) fields. The gray-scale represents the number density of the N393-detected objects. The black solid line indicates zero line emission or absorption, while the blue solid curve represents the 3σ rms scatter selection criteria of LAE candidates as a function of narrowband magnitude. The red dots show the 3σ selected LAE candidates and the upper arrows denote the LAE candidates that were not detected at either U or B band at a 2σ level.

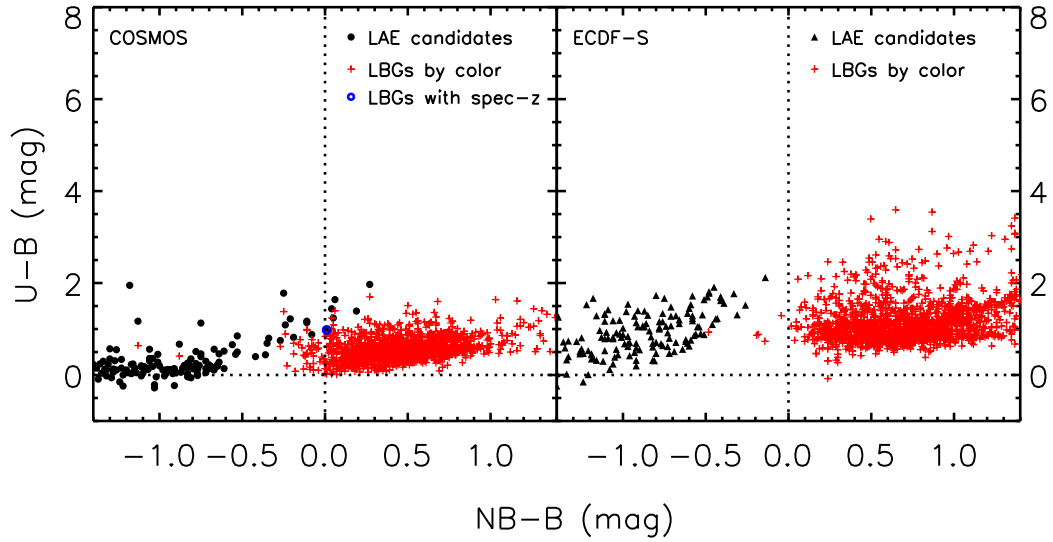


Figure 5. Selection of $z \sim 3$ LBGs by $U-B$ vs. $NB-B$ colors for the COSMOS (left) and ECDF-S (right) fields. The selection criterion $NB - B > 0$ is plotted as a dotted line. The filled circles in the left panel and the filled triangles in the right panel represent LAE candidates. The red crosses are $z \sim 3$ LBGs selected by commonly used broadband LBG technique (Álvarez-Márquez et al. 2016; Hildebrandt et al. 2005) and the blue open circle denotes a $z \sim 3$ LBG that has already been confirmed by spectroscopic observation (Lilly et al. 2007).

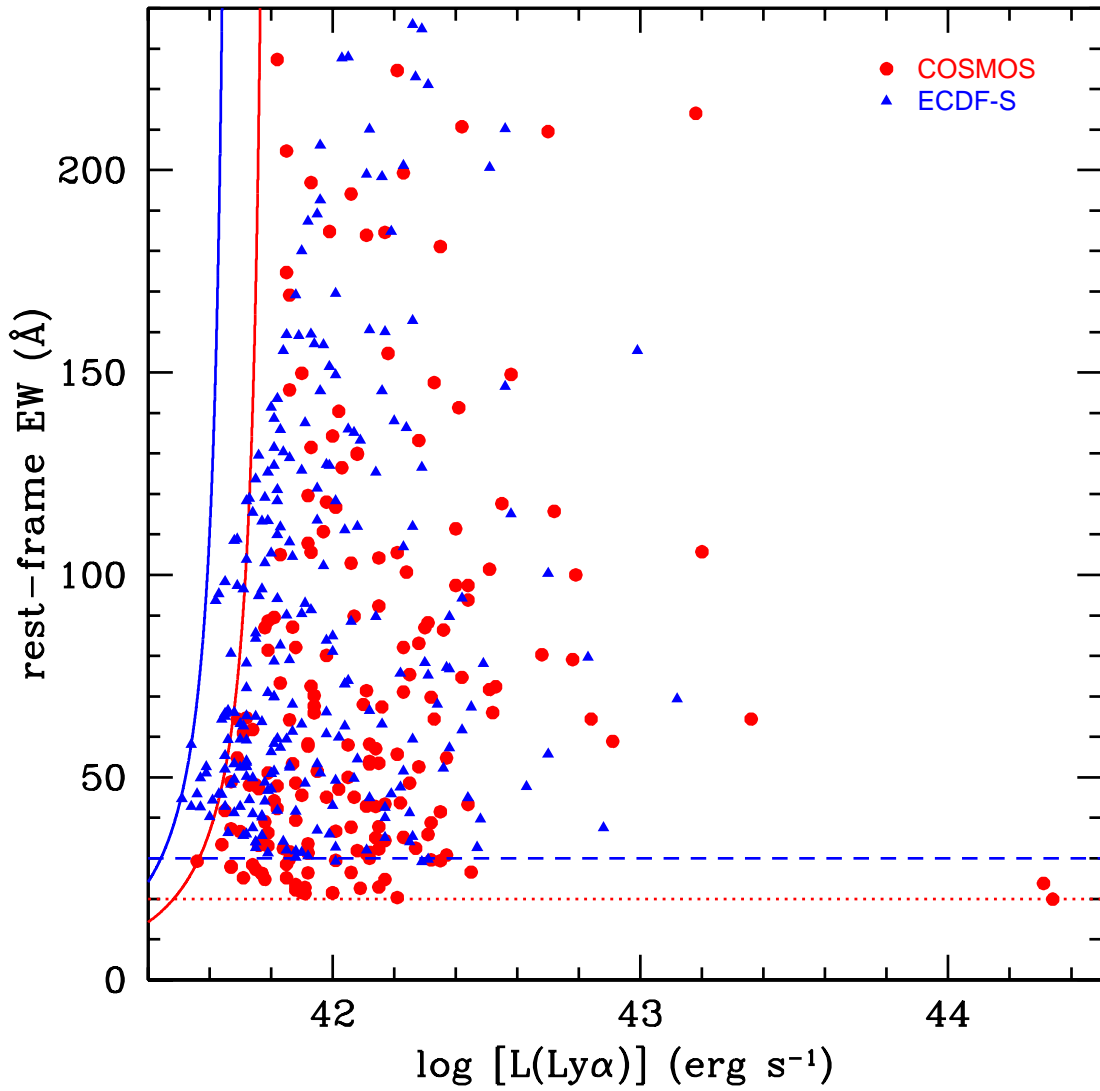


Figure 6. Selection effects in the COSMOS (red circles) and ECDF-S (blue triangles) fields shown in the rest-frame EW versus logarithmic Ly α luminosity plot. The red and blue horizontal lines indicate the color excess selection threshold for the two fields that are equivalent to Ly α EW of 20 Å and 30 Å for the COSMOS and ECDF-S fields, respectively. The red and blue solid curves correspond to the faintest magnitude in the COSMOS and ECDF-S LAEs samples.

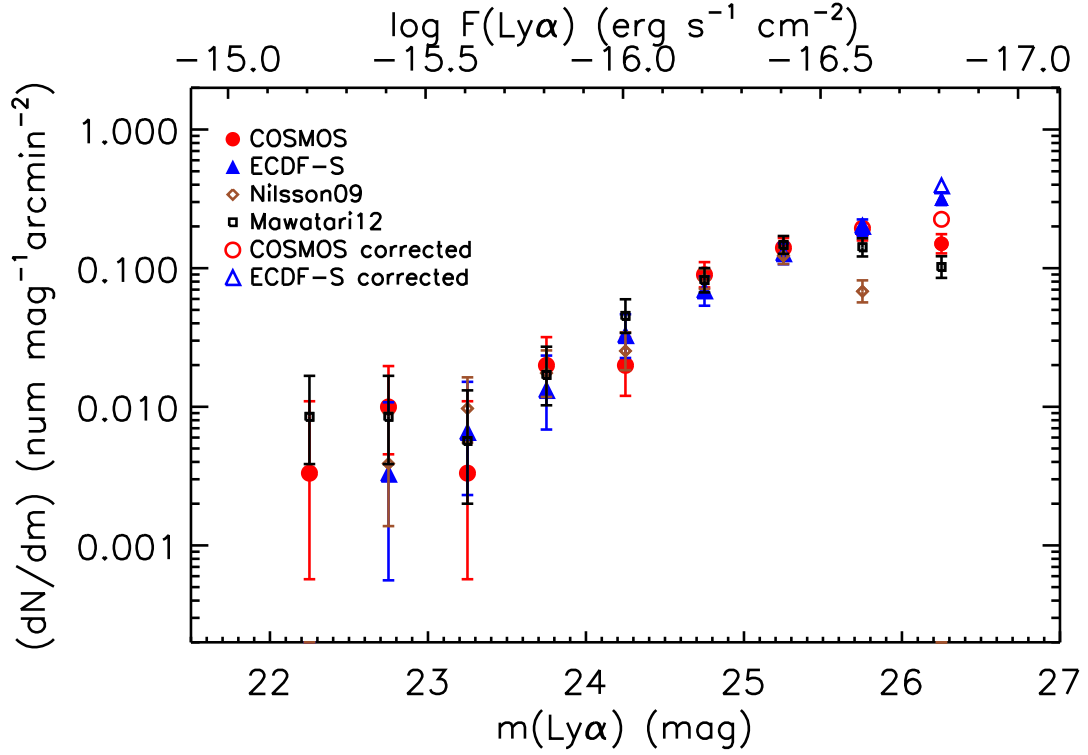


Figure 7. Number counts of LAEs in terms of Ly α magnitude/flux as derived using equation (4) in COSMOS (red filled circles) and equation (7) in ECDF-S (blue filled triangles). The corresponding open symbols represent the completeness-corrected values. LAEs at $z \sim 2.25$ in Nilsson et al. (2009) and LAEs at $z \sim 2.4$ in Mawatari et al. (2012) are plotted in brown diamonds and black squares for comparison.

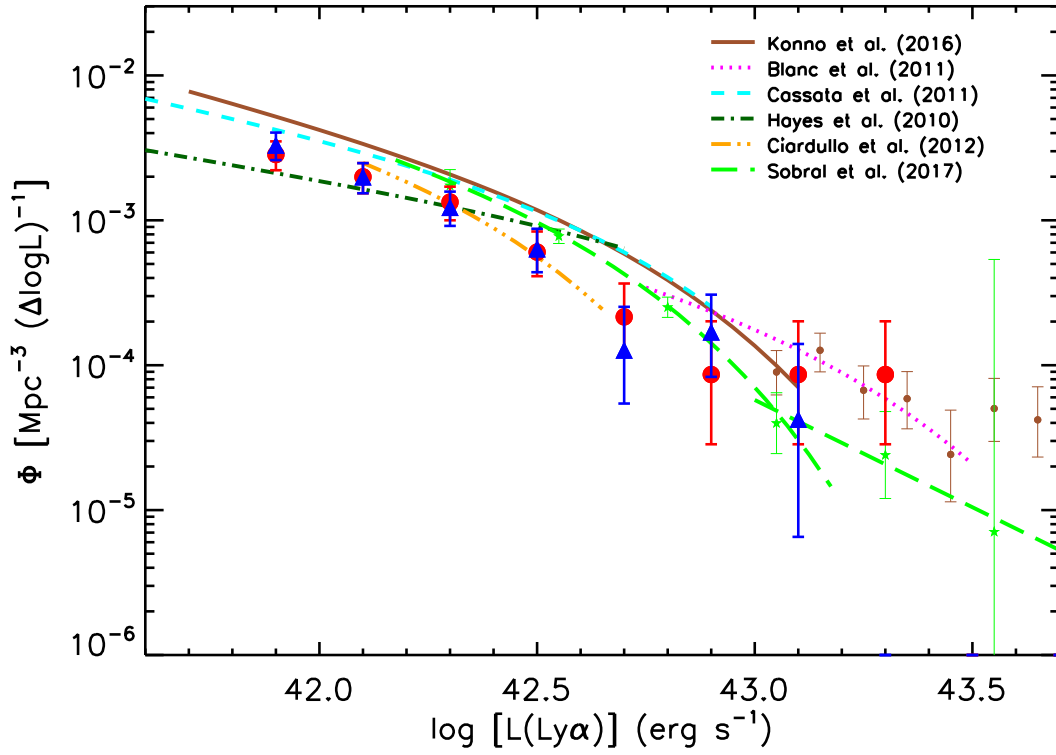


Figure 8. Comparisons of $z \sim 2$ $\text{Ly}\alpha$ luminosity functions in this work and those in the literature. The big data points represent our observed luminosity functions derived using aperture-corrected fluxes and stars-based completeness curves for the COSMOS (red circles) and ECDF-S (blue triangles) fields. The color-coded curves show luminosity functions by different groups, as labeled at the upper-right corner. Data points from Sobral et al. (2017) and the data points with $L(\text{Ly}\alpha) > 10^{43} \text{ erg s}^{-1}$ from Konno et al. (2016) are plotted as small green stars and small brown filled circles, respectively.

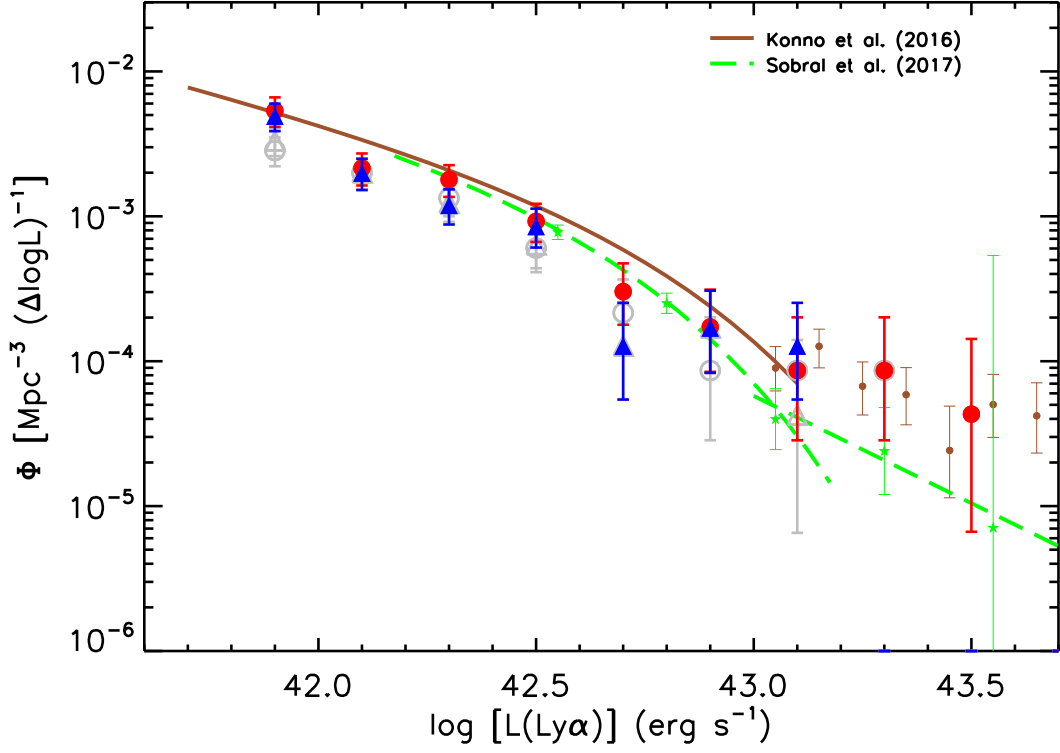


Figure 9. Comparisons of the Ly α luminosity functions based on MAG-AUTO and completeness derived using the reconstructed LAE image (red solid circles for COSMOS and blue solid triangles for ECDF-S) with the Ly α luminosity functions based on the aperture-corrected fluxes and stars-based completeness curves (gray open circles for COSMOS and gray open triangles for ECDF-S) and those in Konno et al. (2016) and Sobral et al. (2017). The best-fit Ly α luminosity functions from Konno et al. (2016) and Sobral et al. (2017) are shown in color-coded curves, as denoted at the upper-right corner. Data points from Sobral et al. (2017) and the data points with $L(\text{Ly}\alpha) > 10^{43} \text{ erg s}^{-1}$ from Konno et al. (2016) are represented by green stars and small brown points, respectively.

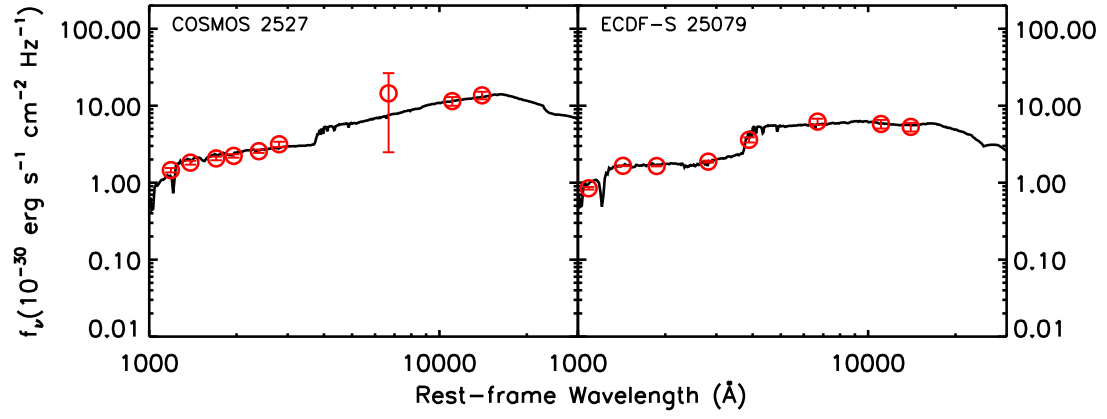


Figure 10. Examples of SED fittings for IRAC-detected LAEs in COSMOS (left) and in ECDF-S (right). The red open circles are the observed flux densities and the black curves are the best-fit SEDs.

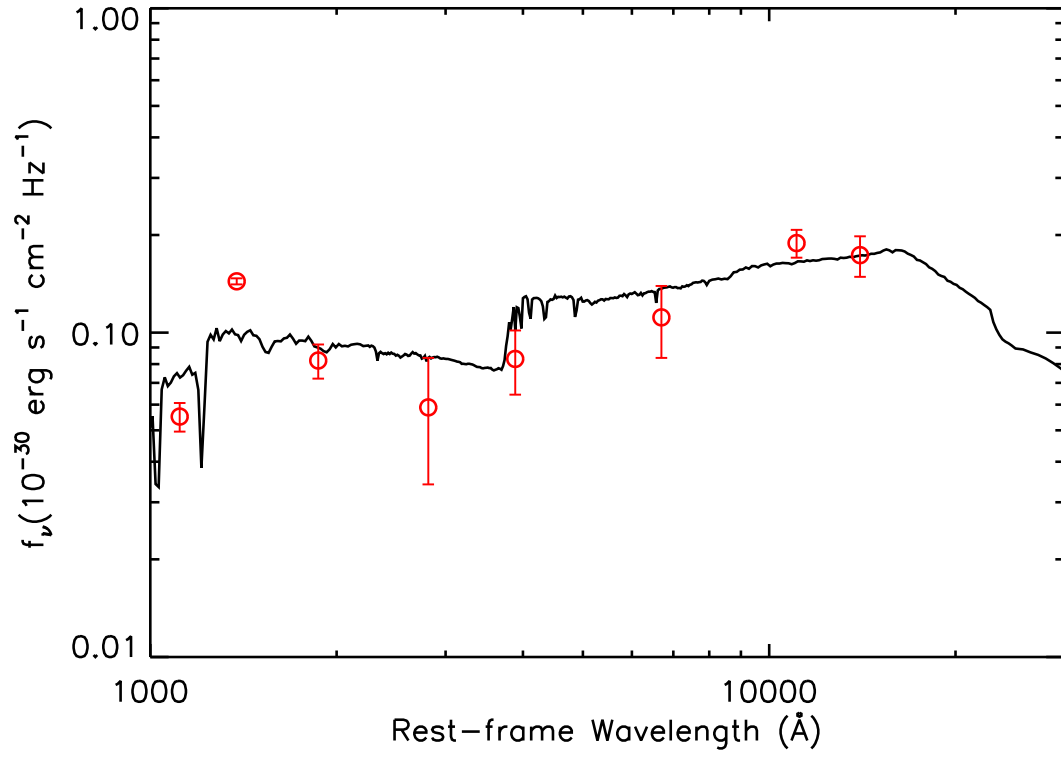


Figure 11. SED fitting of the stacked result of IRAC-undetected LAEs. The red open circles are the stacked flux densities and the black curve represents the best-fit SED.

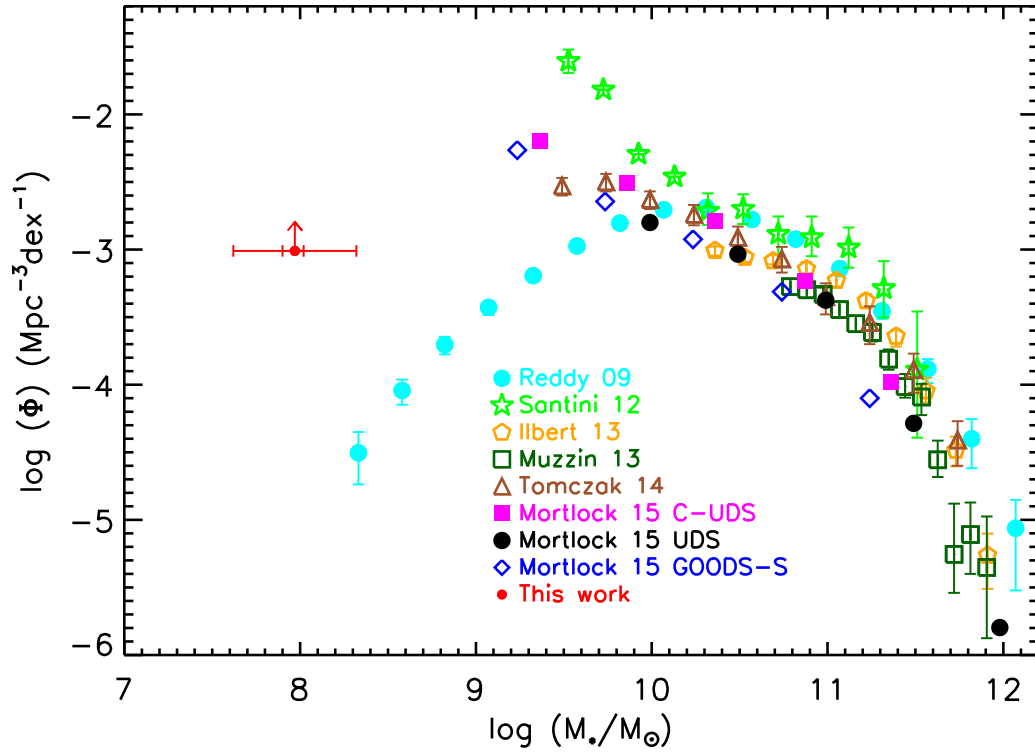


Figure 12. Stellar mass functions at $z \sim 2$. The red symbol represents the constraints from our IRAC-undetected LAEs. The smaller error bars indicate the 1σ errors from the SED fitting, while the larger error bars reflect the possible rms scatter in the stellar mass distribution of the IRAC-undetected LAEs, derived from the rms scatter in the SFRs of these LAEs by assuming that their specific SFRs are the same. Deep stellar mass functions from recent studies as indicated at the lower-right corner are shown for comparison.

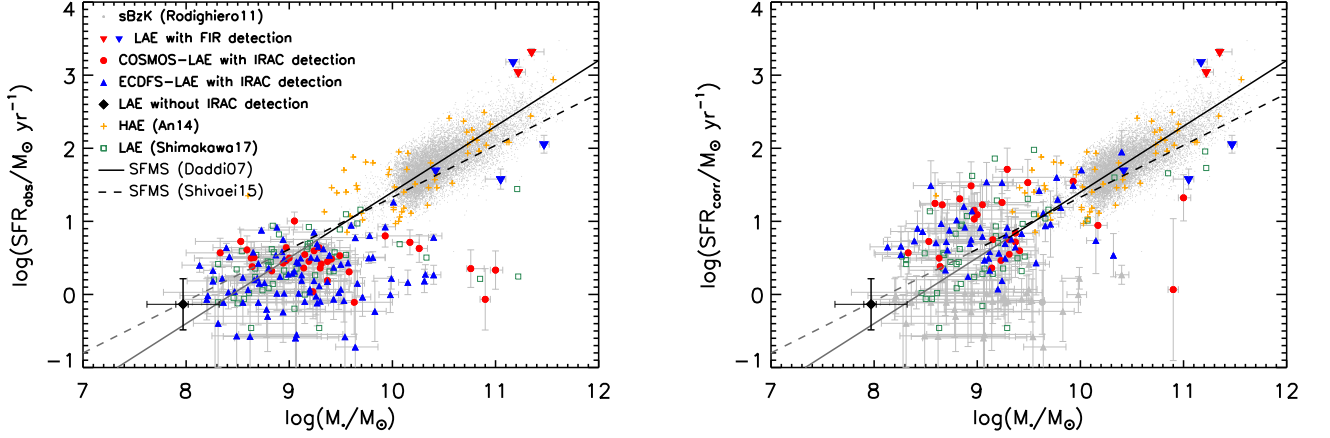


Figure 13. SFR versus stellar mass relation for our IRAC-detected LAEs (red filled circles for COSMOS and blue filled triangles for ECDF-S) and the stacked results (black diamond) for IRAC-undetected LAEs. For the data point representing the stacked results (the black diamond), the horizontal error bars have the same meaning as those in Figure 12, while the vertical error bars indicate the rms scatter in the SFR distribution of the IRAC-undetected LAEs. LAEs at $z \sim 2.5$ from Shimakawa et al. (2017, dark green open squares) are plotted for comparison. BzK-selected star-forming galaxies (gray dots; Rodighiero et al. 2011) and H α emitters in the ECDF-S field (orange crosses; An et al. 2014) are also plotted. Our LAEs with MIR/FIR detections are represented by red (for COSMOS) and blue (for ECDF-S) upside-down triangles. The star formation main sequence relations at $z \sim 2$ from Daddi et al. (2007) and Shivaeei et al. (2015) are plotted as the black solid and dashed lines, respectively. Their extrapolations towards the low-mass regime are plotted using respective lines in gray. *left:* The SFRs for both LAEs in this work and those in Shimakawa et al. (2017) were not corrected for dust attenuations. SFRs of the others were dust corrected as in the original paper. *right:* For IRAC-detected LAEs with B , V , R , I photometry, the SFRs were corrected for dust attenuation using the UV slope and Calzetti law (Calzetti et al. 2000). For IRAC-detected LAEs without B , V , R , I photometry, no dust attenuation was performed and they are plotted as gray symbols. No dust correction was done for the stacked result of the IRAC-undetected LAEs. All the SFRs from the literature were dust-corrected as in the original paper.

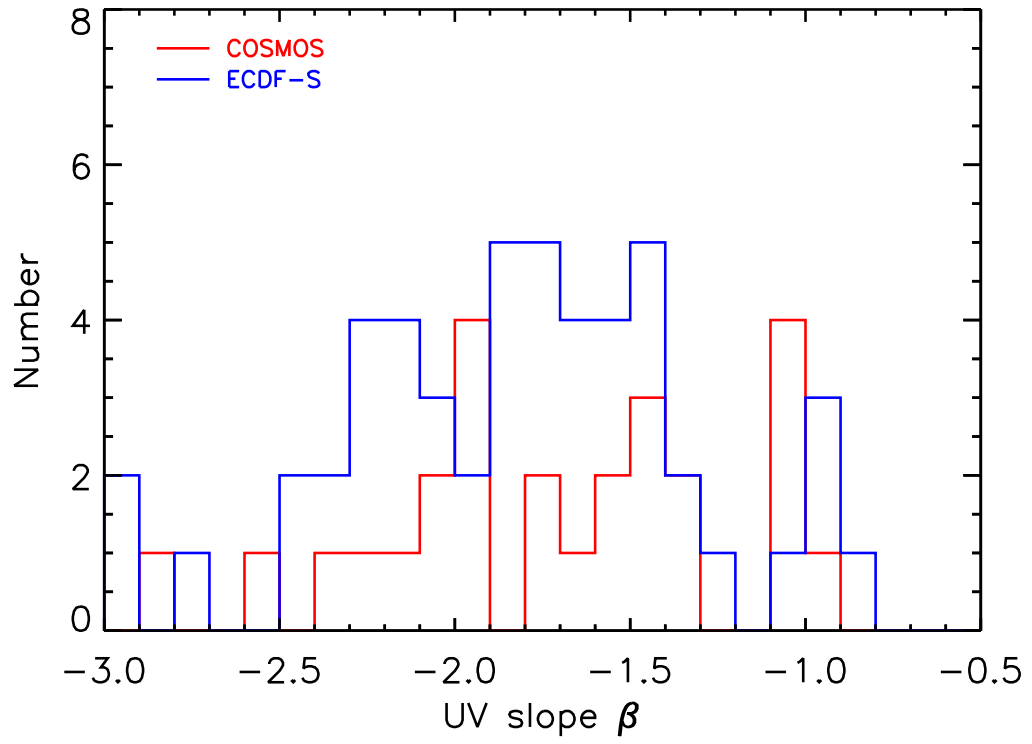


Figure 14. Distribution of the UV slope β for IRAC-detected LAEs with B , V , R and I measurements for the COSMOS (red) and ECDF-S (blue) fields.

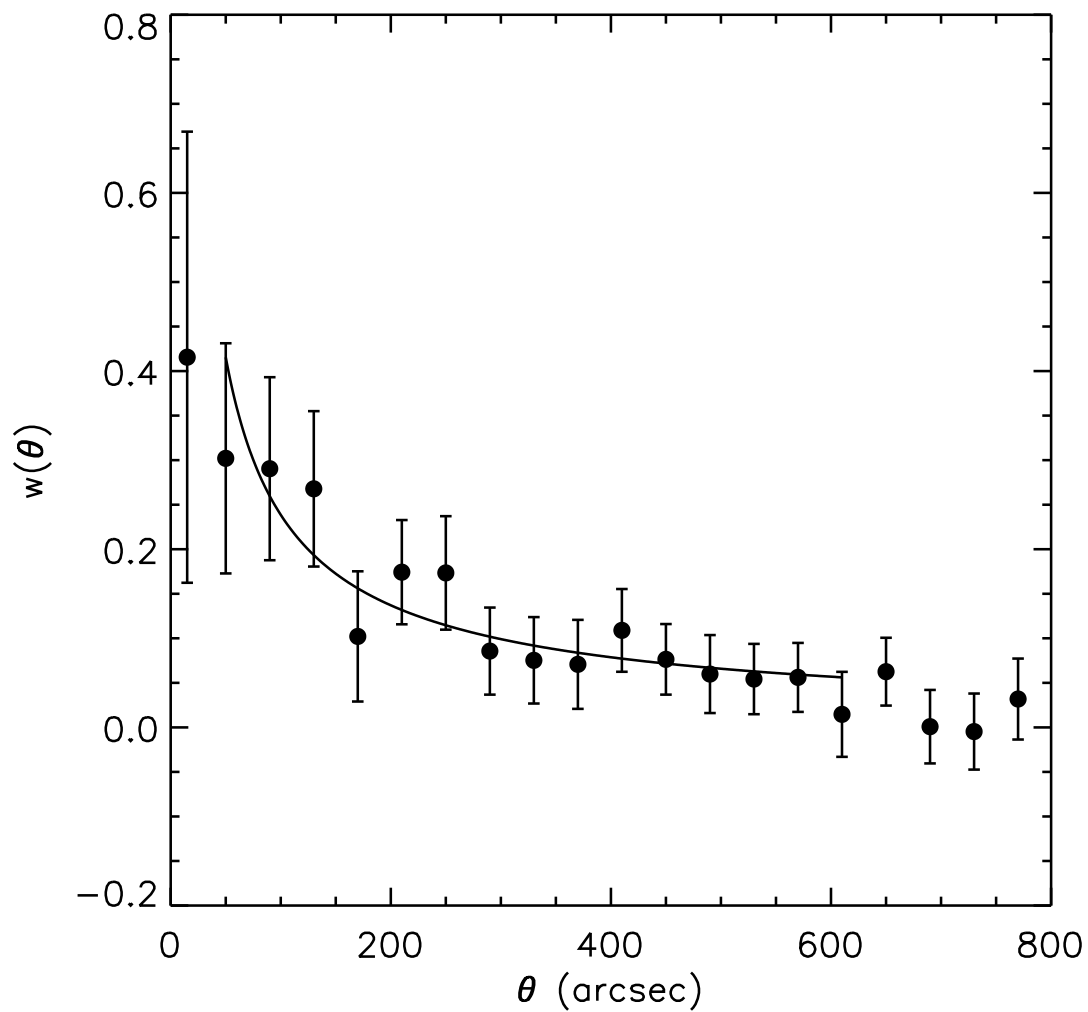


Figure 15. Angular two-point correlation function of the whole sample. The curve is the best power-law fit.